Thinning and surface mass balance patterns of two neighboring debris-covered glaciers in southeastern Tibetan Plateau

Chuanxi Zhao[1,2], Wei Yang[2*], Evan Miles[3], Matthew Westoby[4], Marin Kneib[3,5], Yongjie Wang[2], Zhen He[2,6] and Francesca Pellicciotti[3,4]

[1] College of Earth and Environmental Sciences, Lanzhou University, Lanzhou, 730000, China
[2] State Key Laboratory of Tibetan Plateau Earth System, Environment and Resources (TPESER), Institute of Tibetan Plateau Research, Chinese Academy of Sciences, Beijing, 100101, China
[3] High Mountain Glaciers and Hydrology Group, Swiss Federal Institute, WSL, Birmensdorf, 8903, Switzerland.
[4] Department of Geography and Environmental Sciences, Northumbria University, Newcastle upon Tyne, NE1 8ST, UK
[5] Institute of Environmental Engineering, ETH Zurich, Zurich, 8093, Switzerland
[6] University of Chinese Academy of Sciences, Beijing, 100049, China

Correspondence to: Wei Yang (yangww@itpcas.ac.cn)

Abstract. Debris-covered glaciers are a common feature of the mountain cryosphere in the southeastern Tibetan Plateau. A better understanding of these glaciers is necessary to reduce the uncertainties of the regional water resource variability, and to anticipate potential cryospheric risks. In this study, we quantify seasonal thinning and surface mass balance patterns of two neighboring debris-covered glaciers (23K Glacier and 24K Glacier) in the southeastern Tibetan Plateau with repeated unpiloted aerial vehicle surveys and in-situ measurements (13th Aug. 2019 - 20th Oct. 2020). We observe that the thinning ~~magnitude~~ of 23K Glacier is ~2-7 times greater than that of 24K Glacier for annual and cold periods. The surface velocity of 24K Glacier is higher than that of 23K Glacier (~5-6 times) for all periods. In contrast with the thinning patterns, the surface mass balance patterns of the two glaciers closely agree across the different periods. We find that the surface mass balance distribution strongly correlates with the spatial distribution of debris thickness for both glaciers (23K Glacier: r=0.88; 24K Glacier: r=0.82). Ice cliffs and supraglacial ponds are prevalent on the surface of these glaciers (~4.4-7.2 ± 0.5 %) and overall enhance melt overall (enhancement factor: ~2.5), but do not control the surface mass balance pattern of either glacier. This comparison study of two neighboring glaciers confirms the significance of both glacier dynamic and debris thickness in controlling the thinning and melt for the different debris-covered glaciers of the southeastern Tibetan Plateau in the context of climate change.

1 Introduction

Monsoon-influenced glaciers in the southeastern Tibetan Plateau have experienced more significant mass loss than in most other regions of High Mountain Asia in the past two decades (Kääb et al., 2012; Yao et al., 2012; Brun et al., 2017; Shean et al., 2020; Hugonnet et al., 2021). The percentage of debris-covered area as a proportion of the total glacierised area in the southeastern Tibetan Plateau was estimated at ~17-19%, which exceeds the percentage of debris-covered glacier area at the global scale (~4.4%-7.3%; Scherler et al., 2018; Herreid and Pellicciotti, 2020). A better understanding of the evolution and

mass balance patterns of debris-covered glaciers in the southeastern Tibetan Plateau is essential for constraining changes in regional water resources (Zhang et al., 2011; Neckel et al., 2017). Because proglacial lakes can develop on or in front of debris-covered glaciers (Wang et al., 2011; Allen et al., 2019; Racoviteanu et al., 2022), and because glacier thinning may affect slope stability (Kääb et al., 2021; An et al., 2022; Zhao et al., 2022), expanding this knowledge base may also inform understanding of mountain geohazards.

The presence of debris can Influence the response of glacier to climate change. If the supraglacial debris is more than a few centimeters in thickness, it will provide a melt-buffering effect (Østrem, 1959; Nakawo et al., 1999; Nicholson and Benn, 2006; Reid and Brock, 2010; Anderson and Anderson, 2016; Yang et al., 2017). However, several satellite remote sensing studies have found similar thinning rates for debris-free and debris-covered glaciers (Kääb et al., 2012; Gardelle et al., 2013; Pellicciotti et al., 2015; Brun et al., 2019). There is even a higher thinning rate of debris-covered- compared to debris-free glaciers in the Lahaul and Spiti region, Indian Himalaya (Vincent et al., 2013) and several studies also confirm the strong surface thinning of debris-covered glaciers in the southeastern Tibetan Plateau (-0.52- -0.83 m a^{-1}; Neckel et al., 2017; Ke et al., 2020). This phenomenon has been referred to as the "debris-cover anomaly" (Pellicciotti et al., 2015; Vincent et al., 2016). Ice cliffs and supraglacial ponds could partly explain this anomaly, because they are directly exposed to incoming radiations and therefore act as melt "hotspots" (Sakai, 1998, 2002; Reid and Brock, 2014; Juen et al., 2014; Steiner et al., 2015; Buri et al., 2016; Miles et al., 2016; Miles et al., 2018; Buri et al., 2021). The areas around by cliffs and ponds are characterized by high melt rates relative to surrounding debris-covered area (not containing ice cliffs and ponds) based on the differencing of high-resolution digital elevation models (DEMs) and energy-balance modelling (Thompson et al., 2016; Brun et al., 2018; Miles et al., 2018, 2022; Buri et al., 2016, 2021; Kneib et al., 2022; Sato et al., 2021; Mishra et al., 2021; Miles et al., 2022). However, some studies have found that the thicker debris cover has a larger effect on total thinning than the enhanced ice ablation from ice cliffs and supraglacial ponds area (e.g., Hambrey et al., 2008; Vincent et al., 2016; Brun et al, 2018; Anderson et al, 2021a). Additionally, glacier dynamics play an essential role in debris-covered glacier elevation change, and the rapid thinning of debris-covered glaciers is speculated to be partly caused by declining ice flow (Nuimura et al., 2017; Brun et al., 2018; Anderson et al., 2021a, 2021b; Rounce et al., 2021). However, this has been evaluated with high accuracy at very few sites, none of which are in the southeast Tibetan Plateau.

These hypotheses (additional melt at hotspots area or extra thinning from reduced ice supply) therefore need to be supported with high resolution data to account for the local effects of these melt hotspots. Since ice cliffs and supraglacial ponds tend to have a relatively small area and be very changeable (Miles et al., 2017; Kneib et al., 2021), it is challenging to accurately track their evolution over time and quantify their contribution to melt (Mishra et al., 2021; Kneib et al., 2022). Because of these challenges, studies which have investigated their spatial distribution, dynamics, and melt contribution have typically utilized unpiloted aerial vehicle (UAV) or very high-resolution optical satellite data (Immerzeel et al., 2014; Brun et al., 2016; Brun et al., 2018; Mölg et al., 2019; Anderson et al., 2021a; Kneib et al., 2021, 2022; Mishra et al., 2021; Sato et al.,

2021), which can infer detailed observations of local processes (e.g., Westoby et al., 2020). Compared with the use of the UAVs, *in-situ* observations have the shortcoming of limited spatial representation, and remote sensing data have insufficient resolution and are vulnerability to cloudy and rainy weather. Therefore, the UAV technology is widely applied in glaciological studies, including in debris-covered glacier settings (Hugenholtz et al., 2013; Immerzeel et al., 2014; Kraaijenbrink et al., 2016; Wigmore and Mark, 2017; Fugazza et al., 2018; Rossini et al., 2018; Bash and Moorman, 2020; Westoby et al., 2020; Cao et al., 2021; Mishra et al., 2021; Xu et al., 2022). High-precision digital elevation models (DEMs) and orthophotos can be obtained relatively easily from UAV images processed using Structure-from-Motion (UAV-SfM) with multi-view stereo photogrammetry (Westoby et al., 2012; Benoit et al., 2019). However, there are few studies that estimate the seasonal or annual surface mass balance (SMB) of debris-covered glaciers based on repeated UAV data.

Here we systematically compare the glacier change patterns of two neighboring debris-covered glaciers, 23K Glacier and 24K Glacier, in the southeastern Tibetan Plateau for the period 13th August 2019 to 22nd October 2020 by change detection applied to high-resolution repeated DEMs and orthoimages acquired via UAV-SfM surveys and *in-situ* measurements. The glaciers are located in the same catchment and climatic setting, but the topography of the glaciers, as well as their dynamic behavior and supraglacial debris thickness differs considerably. The objective of this study is to explore the factors that control the inter-glacier variability in surface thinning (dh) and surface mass balance (SMB) patterns of these two glaciers, with a view to advance the understanding of the key mechanisms that control debris-covered glacier changes in the southeastern Tibetan Plateau, and to assess the two different hypotheses at the glacier scale (additional melt at hot spots area or extra thinning from reduced ice supply) that contribute to the anomalous thinning of debris-covered glaciers.

2 Study area

23K (~4 km^2) and 24K (~2 km^2) Glaciers are located in the southeastern Tibetan Plateau (~29.77° N, 95.70° E; Fig. 1)., and are mainly affected by two streams of humid air: the Bay of Bengal Vortex (in Spring) and the Indian Summer Monsoon system (in Summer), respectively (Ye and Gao, 1979; Yang et al., 2013; Yang et al., 2016). Thus, the monthly precipitation distribution exhibits a double-peak pattern occurring in both spring and summer (Yang et al., 2013). This is significantly different to the glacier regime on the Tibetan Plateau, which are so-called 'summer accumulation' type (Fujita et al., 2000; Maussion et al., 2014). Regional geodetic mass balance studies indicate that the magnitude of ice loss in the region exceeds the average for High Mountain Asia (Kääb et al., 2012; Yao et al., 2012; Brun et al., 2017; Shean et al., 2020; Hugonnet et al., 2021) in the past 20 years, also affecting debris-covered glaciers. 23K and 24K Glaciers are located on the northern slopes of the Gangrigabu Mountains, ~23 kilometers and 24 kilometers, respectively, from Bomi City (Yang et al., 2017). 23K Glacier spans an altitudinal range of 3,760 to 5,437 m a.s.l. and flows initially toward the south-east before turning to the northeast in the ablation zone (Fig. 1a). In contrast, 24K Glacier flows to the northwest, and spans an altitudinal range of 3,900 to 5,621 m a.s.l. Both glaciers are partly covered by a layer of rock debris (Fig. 1a, 1c) and the debris-covered area represents approximately 34% and 41% of the total area for 23K Glacier and 24K Glacier respectively based on satellite data

(Pléiades-1A false-color image from 2021-09-20, 2m resolution). The terminus retreat patterns of the two glaciers are also conspicuously different: the terminus of 23K Glacier appears largely stagnant and is enclosed by a latero-terminal moraine complex, while the terminus of 24K Glacier presents of a large ice cliff, and which is bounded by lateral moraines (Fig. 1c, 1d). Data from an automatic weather station (AWS, 3900 m a.s.l., running between June and September 2016) on 24K Glacier indicates a warm and humid climate, with mean temperature and total precipitation reaching ~9 ℃ and ~1700 mm, respectively (Yang et al., 2017; Fugger et al., 2022).

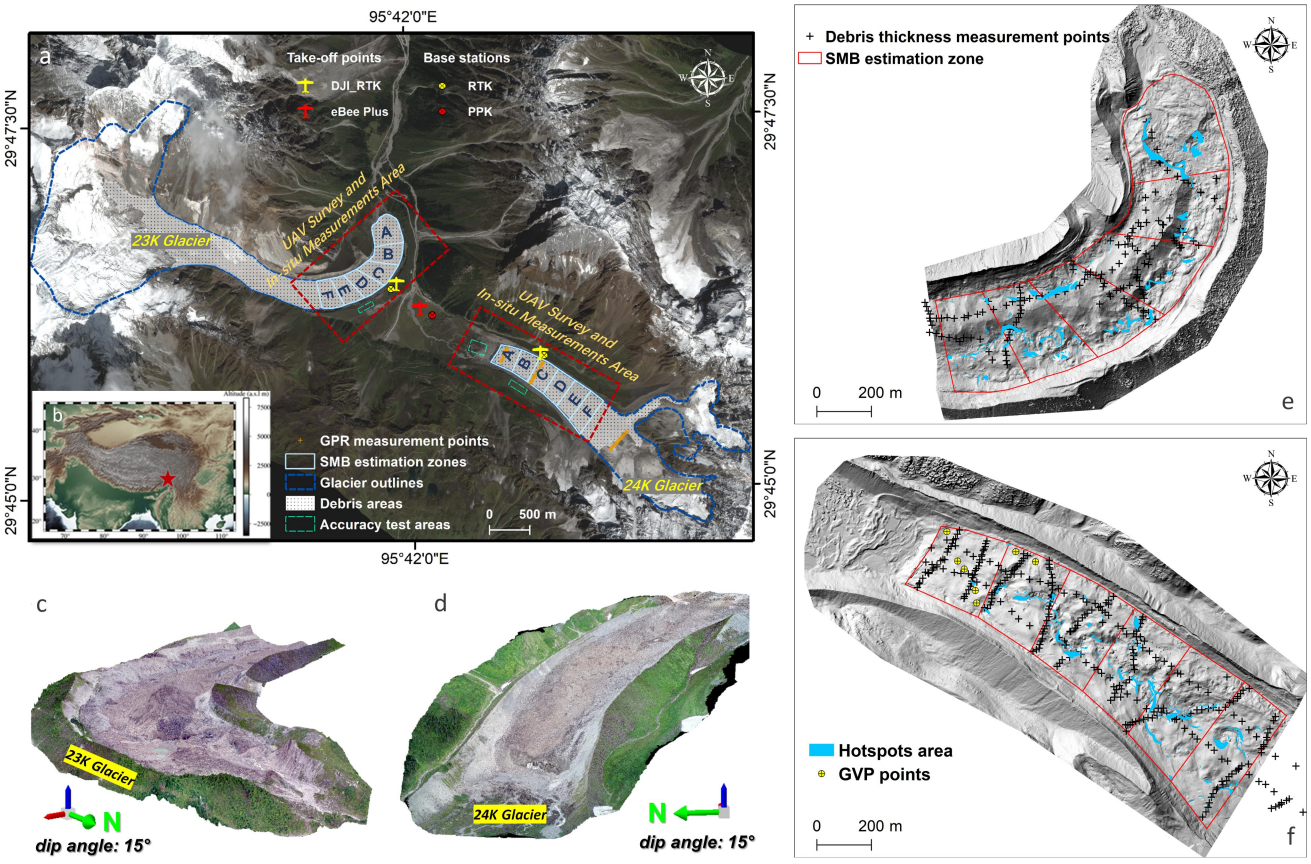

Figure 1: (a) Overview of the 23K Glacier and 24K Glacier basin including the UAV survey area, accuracy test areas, *in-situ* measurement locations (GVPs, GPR, debris thickness measurements), surface mass balance estimation zones (zones A-F) and glacier outlines (background image from Pléiades-1A false-color image from 2021-09-20). © CNES 2021, Distribution Airbus D&S. (b) Geographic location of the study area. (c-d) UAV-derived three-dimensional images for the two glaciers. (e-f) Spatial distribution of the surface mass balance estimation zones of the two glaciers (e: 24K Glacier; f: 23K Glacier), debris thickness measurement points (in June 2019), and distribution of ice cliffs & supraglacial ponds (based on 2020 orthomosaics).

3 Data and Methods

3.1 UAV flights and data processing

Optical imagery of the glacier surface and its immediate surroundings was acquired using UAVs during four field campaigns conducted between August 13th 2019 and October 22nd 2020 (Table 1). We used an eBee Plus aircraft with built-in GNSS PPK functionality in October 2019, August 2020, October 2020 surveys and DJI Phantom 4 RTK in August 2019 survey to capture the high-resolution annual and seasonal patterns of glacier thinning and surface displacement.

The eBee Plus (Fig.S1a) is a fixed-wing UAV that has a 20-megapixel RGB digital compact camera (SenseFly S.O.D.A.). The flight management software eMotion3® was used for flight planning. The DJI Phantom 4 RTK is a rotary-wing UAV (Fig.S1c) equipped with a 1-inch, 20-megapixel CMOS camera. In this study, all longitudinal and lateral image overlaps were set to 65% and 80%, respectively. The flight lines for the eBee Plus and DJI Phantom 4 RTK maintained a relatively constant survey height above the glacier surface, which resulted in a constant ground resolution for each survey. A Huaxing A10 GNSS GPS was used as a static base station (Fig.S1b; fixed position for different surveys), and these data were attached to EXIF metadata of every geotagged image (Yang et al., 2020) and thereby integrated into a Post-Processed Kinematic (PPK) correction workflow to improve the accuracy of the UAV-SfM reconstruction. The DJI Phantom 4 real-time kinematic (RTK) UAV was permanently connected to a GNSS receiver (D-RTK 2, Fig. S1d), so that each survey image already had its high-precision position information embedded (i.e., no post-processing required). The geotagged UAV images were used to create orthomosaics and DEMs using the SfM-based photogrammetric software Pix4Dmapper version 4.3.31.

To assess the final positional accuracy of the UAV-derived DEMs and outputs, seven ground validation points were laid out in the vicinity of *in-situ* measurements (Fig.1a) on the surface of 24K Glacier in October 2020 (synchronized with the October 2020 UAV survey). We used a Huaxing A10 dGPS system to measure the position (XYZ) of each ground validation point. The horizontal accuracy of the dGPS is ± 8 mm and the vertical accuracy is ± 15 mm. By comparing the ground validation point measurements with the UAV-derived orthomosaics and DEMs, we obtain absolute XYZ accuracies for the October 2020 UAV-SfM survey product (Table 2). While ground validation points were not used for the other UAV-SfM surveys, the accuracies of all UAV-SfM products were indirectly assessed by comparing the horizontal (XY) and vertical errors (Z) between all orthomosaics and DEMs (Table 3). The horizontal (XY) error was estimated by measuring the displacements of 25 benchmark boulders located on stable off-glacier terrain. For the vertical (Z) error, we calculated the elevation difference over stable terrain, as outlined in Figure 1a.

Table 1: UAV photogrammetric flights used for the acquisition of glacier images.

Time	Flight type	Glacier	Number of Images	Flight altitude above ground (m)	Ground resolution (cm)	Coverage area (km^2)	Flight time (Beijing time)
13th Aug. 2019	RTK	23K	558	298	7.0	2.3	13:29-14:14
		24K	468	315	7.4	2.0	17:00-18:22
12th Oct. 2019	PPK	23K	743	243*	6.9	6.9	11:25-12:34
		24K	445				10:13-11:03
20th Aug. 2020	PPK	23K	128	434	10.2	3.1	12:07-12:26
		24K	160	536	12.6	3.7	11:11-11:35
22nd Oct. 2020	PPK	23K	188	344	8.1	2.4	10:37-10:59
		24K	346	374	8.8	3.8	8:57-9:37

3.2 *In-situ* observations and measurements

To evaluate the role of debris on surface mass balance patterns of both glaciers, debris thickness was manually measured by digging pits at selected sites in June 2019 (Fig. 1d, 1e). For 23K Glacier, a total of 157 locations were measured within the elevation range of 3,740-3,880 m a.s.l. For 24K Glacier, we measured a total of 349 points from the glacier terminus to 4,250 m a.s.l. The uncertainty of the manual measurement of the debris thickness was assumed to be 2 cm.

In October 2019, three ice thickness cross-sections (two in the debris-covered area and one in the debris-free area, Fig.1a and Fig. S2) were measured on 24K Glacier using a Kentech ground penetrating radar (GPR) monopulse transmitter with 2.5 MHz antennas. The *in-situ* ice thickness measurements were used to correct the 24K Glacier distributed ice thickness from Farinotti et al. (2019) using linear regression (Fig. S2; Kneib et al., 2022).

3.3 Thinning (d*h*) patterns, glacier dynamics and glacier driving stress

We compared the thinning (d*h*) and velocity patterns of 23K and 24K Glaciers on an annual and on a seasonal timescale. The period between August 2019 and August 2020 (373 days, mean temperature at AWS: 1.66 ℃) was selected for the annual timescale analysis. The annual rates were adjusted according to the ratio of days (366/373) to make this result (13th Aug. 2019 - 20th Oct. 2020, 373 days) closer to that of the natural year (366 days). For the seasonal analysis, we refer to the period October 2019-August 2020 (313 days, mean temperature: 0.42 ℃) as the 'cold period' and the period August 2020-October 2020 (63 days, mean temperature: 8.68 ℃) as the 'warm period'. We applied the Post-Processed Kinematic (PPK) and real-time kinematic (RTK) GPS correction technologies and ensured that the static base stations were fixed at the same location for different surveys, which lead to DEMs with only very small minor offsets in XYZ (Yang et al., 2020). Therefore, we did not perform the co-registration of DEMs for the thinning (d*h*) calculation. For each period the thinning pattern was obtained by 2.5D DEM differencing in ArcGIS 10.4.

A spatially distributed estimate of XY surface displacements was obtained for each period by applying a Normalized Cross Correlation algorithm to the multidirectional 0.15 m-resolution DEM hillshades using ImGRAFT (Messerli and Grinsted, 2015). A search window of 10 × 10 pixels (1.5 × 1.5 m) was used to compute the magnitude and directions of the displacement vectors. The surface displacements greater than 30 m were considered as noise and were filtered out. Due to the high-resolution velocity data and the small number of gaps (<5%), we interpolated the velocity values in the data gaps using nearest neighbor interpolation.

The glacier driving stress was calculated as (Cuffey and Paterson, 2010):

$$D_{stress} = \rho_i \cdot g \cdot h \cdot sin\,\alpha_s, \quad (1)$$

where D_{stress} is the glacier driving stress, ρ_i is the density of ice (917 kg m^3), g is the gravitational acceleration (9.81 m s^{-2}), h is the ice thickness (in m), and α_s is the glacier slope obtained from the AW3D30 (30 m-resolution) DEM (Tadono et al., 2014) smoothed with a Gaussian filter (8 pixels window) to remove effects from local variations in surface topography (Brun et al., 2018).

3.4 Surface mass balance (SMB) of UAV survey area

To investigate the magnitude and the distribution of the surface mass balance, each glacier was divided into six zones (A-F) and each zone was used as a separate section for the surface mass balance estimation. Each surface mass balance estimation zone was outlined manually, perpendicular to the main glacier flow line and with a similar area (Fig. 1a). To extract the melt contribution from the ice cliffs and ponds, we flow-corrected the DEMs following Brun et al. (2018). To perform the flow correction, we used orthomosaics and DEMs from the August 2020 UAV-SfM surveys as a reference for each glacier, to which the August 2019, October 2019 and October 2020 UAV-derived data were flow-corrected. Corrections in XY were made using the ArcGIS georeferencing tool to manually track the surface flow for each given period by using surface tie points (mainly large boulders). For each correction period, the number of tie points was sufficiently large (> 75) and the tie points were well-distributed across the glacier surface to ensure a spatially representative correction, using a spline-based transformation. The resulting XY flow-corrected elevation change (dh_c, in m) is therefore equal to the sum of the surface mass balance ($\dot{b}$, negative value in the ablation area, in m) and the mean vertical displacement (ω, in m):

$$dh_c = \dot{b} + \omega, \quad (2)$$

$$\omega = \omega_s + \omega_e\,, \quad (3)$$

$$\omega_s = u_s \cdot tan\,(\alpha_m)\,, \quad (4)$$

$$\omega_e = \frac{\Delta q}{A}, \quad (5)$$

$$\Delta q = q_{n+1} - q_n, \quad (6)$$

$$q = \mu \cdot h_q \cdot v \cdot l, \quad (7)$$

Where ω_s (in m) corresponds to the elevation change resulting from the horizontal flow-correction of the DEMs, u_s (in m) is the mean horizontal surface displacement and α_m (in °) is the mean surface slope of a given zone. ω_e (in m) corresponds to the flux divergence. A (in m^2) is the area of the zone and Δq (in m^3) is the ice flux difference at a given period. Where q_{n+1} and q_n are the ice flux entering and leaving the estimation zone at a given period. q (in m^3) is the ice flux through a glacier cross-section. μ is a coefficient to convert the surface velocity into a depth-averaged velocity which we assumed to be equal to 0.9 following Miles et al. (2018), h_q (in m) is the ice thickness for the corresponding cross-section, v (in m) is the surface displacement component normal to the cross sections line, l (in m) is the width of the cross-section.

The following equation was used to evaluate the uncertainty of surface mass balance ($\sigma_{\dot{b}}$) for each zone:

$$\sigma_{\dot{b}} = \sqrt{{\sigma_{dh_c}}^2 + {\sigma_{\omega}}^2}, \quad (8)$$

The uncertainties of dh_c and u_s (also for v) were obtained by calculating the mean surface elevation difference and displacement the non-glacial test areas. They were determined as 0.09 m and 0.25 m respectively by averaging the values over all periods.

The equations below were applied in the uncertainty of vertical component of velocity (σ_ω):

$$\sigma_\omega = \sqrt{{\sigma_{u_s}}^2 + {\sigma_{\alpha_m}}^2 + {\sigma_{\omega_e}}^2} \quad (9)$$

$$\frac{\sigma_{\omega_e}}{\omega_e} = \sqrt{\left(\frac{\sigma_{\Delta q}}{\Delta q}\right)^2 + \left(\frac{\sigma_A}{A}\right)^2}, \quad (10)$$

For the uncertainty associated with the slope correction, we assumed a 2° uncertainty in the slope (α_m). We assumed the uncertainty of zone area （A） to be ± 20 m from the outlines with the buffer method (Bolch et al., 2010; Miles et al., 2018). The uncertainty of ice flux difference ($\sigma_{\Delta q}$):

$$\sigma_{\Delta q} = \sqrt{{\sigma_{q_{n+1}}}^2 + {\sigma_{q_n}}^2}, \quad (11)$$

σ_q (m^3) is the uncertainty of ice flux through a glacier cross-section, given by:

$$\frac{\sigma_q}{q} = \sqrt{\left(\frac{\sigma_v}{v}\right)^2 + \left(\frac{\sigma_\mu}{\mu}\right)^2 + \left(\frac{\sigma_{h_q}}{h_q}\right)^2}, \quad (12)$$

where the uncertainty of ratio μ (column-averaged velocity/surface velocity) is assumed as 0.1 (Cuffey and Paterson, 2010; Miles et al., 2018). The uncertainty in h_q is ~10-35 m (26%) for 23K Glacier (Farinotti et al., 2019) and is assumed to be equal to 12 m for the corrected 24K Glacier (Fig. S2a) ice thickness uncertainty.

3.5 Ice cliffs and supraglacial ponds outlines and melt contribution

In this study, the proportion of ice cliffs and supraglacial ponds areas within each surface mass balance estimation zone was calculated to better understand the surface mass balance patterns on both glaciers. We manually extracted ice cliffs and supraglacial ponds outlines from the flow-corrected orthomosaics (August 2020 and October 2020; August 2019 and August 2020; October 2019 and August 2020). The outlines of the ice cliffs and supraglacial ponds area for each zone were combined into one polygon feature by taking the union of the areas of these features (Brun et al., 2018). In this way, we can effectively measure surface change in these ice cliffs and supraglacial ponds areas, thereby providing us with an upper-bound estimate of the total contribution of ice cliffs and ponds to the surface mass balance (Kneib et al., 2022; Mishra et al., 2022). We conservatively assumed the uncertainty of areas density of ice cliffs and supraglacial ponds to be equal to 0.5% (Brun et al., 2018; Steiner et al., 2019). The enhancement factor was calculated ~~to quantify such difference in melt enhancement between the two glaciers' ice cliffs and supraglacial ponds area and sub-debris area during all periods~~, which we define as the ratio of the ice cliffs and supraglacial ponds area surface mass balance rate to the sub-debris area surface mass balance rate (Brun et al., 2018, Buri et al., 2021, Miles et al., 2022).

4 Results

4.1 UAV products accuracy

The uncertainties in the UAV measurements , reported as mean absolute deviation in the X, Y and Z directions are 0.14 ± 0.11 m, 0.09 ± 0.11 m, and 0.24 ± 0.18 m respectively (Table 2). The vertical uncertainty is twice as high as the horizontal uncertainty, which is in agreement with the findings of other studies (James et al., 2017; Li et al., 2019).

Table 2: XYZ geolocation accuracy of UAV-SfM orthomosaic and DEM (22nd Oct. 2020) for the two glaciers, based on the dGPS measurements of the 7 GVPs.

	X (m)	Y (m)	Z (m)

23K&24K Glaciers	Mean	0.14	0.09	0.24
	Std	0.11	0.11	0.18

The average XY errors for three survey pairs (Aug. 2019 *vs* Oct. 2019, Oct. 2019 *vs* Aug. 2020 and Aug. 2020 *vs* Oct. 2020) were 0.07 ± 0.06 m and 0.08 ± 0.06 m respectively (Table 3). The relative vertical (Z) errors between DEMs were ≤0.09 m for all pairs, which is appropriate for resolving fine-scale surface change for glaciological analysis.

Table. 3: XYZ errors between different orthomosaics/DEMs for the two glaciers using the fixed benchmark boulders and validation areas.

		23K&24K Glaciers		
		Aug. 2019-Oct. 2019	Oct. 2019-Aug. 2020	Aug. 2020-Oct. 2020
X (m)	Mean	0.07	0.08	0.07
	Std	0.06	0.07	0.06
Y (m)	Mean	0.06	0.09	0.09
	Std	0.04	0.06	0.05
Z (m)	Mean	0.09	0.08	0.09
	Std	0.07	0.04	0.08

4.2 Spatio-temporal variability of thinning (d*h*) patterns

The thinning during different periods (annual: Aug. 2019-Aug. 2020, cold: Oct. 2019- Aug. 2020, warm: Aug. 2020-Oct. 2020) for the two glaciers is shown in Figure 2 and Table 4. The annual thinning rate of 23K Glacier in the survey area was -2.3 ± 0.1 m a^{-1}, whereas the thinning rate of 24K Glacier was -1.2 ± 0.1 m a^{-1} (Fig. 2a, d). During the cold period (October 2019-August 2020), the average thinning over 23K and 24K Glacier survey area were -1.5 ± 0.1 m and -0.2 ± 0.1 m, with an average daily thinning of -0.5 ± 0.03 cm d^{-1} and -0.1 ± 0.03 cm d^{-1}, respectively (Fig. 2b, 2e).. During the warm period (August 2020-October 2020), the magnitude of the thinning of both glaciers was very similar; 23K and 24K Glacier were -0.7 ± 0.1 m and -1.0 ± 0.1 m, with an average daily thinning of -1.2 ± 0.03 cm d^{-1} and -1.6 ± 0.03 cm d^{-1}, respectively (Fig. 2c, 2f).

Table. 4: Total thinning and its daily rate for 23K & 24K Glaciers during different periods.

		Aug. 2019- Aug. 2020	Oct. 2019-Aug. 2020	Aug. 2020-Oct. 2020
23K Glacier	Thinning (m)	-2.3 ± 0.1	-1.5 ± 0.1	-0.7 ± 0.1
	Daily rate (cm d^{-1})	-0.6 ± 0.03	0.5 ± 0.03	-1.2 ± 0.03
24K Glacier	Thinning change (m)	-1.2 ± 0.1	-0.2 ± 0.1	-1.0 ± 0.1
	Daily rate (cm d^{-1})	-0.3 ± 0.03	-0.1 ± 0.03	-1.6 ± 0.03

250

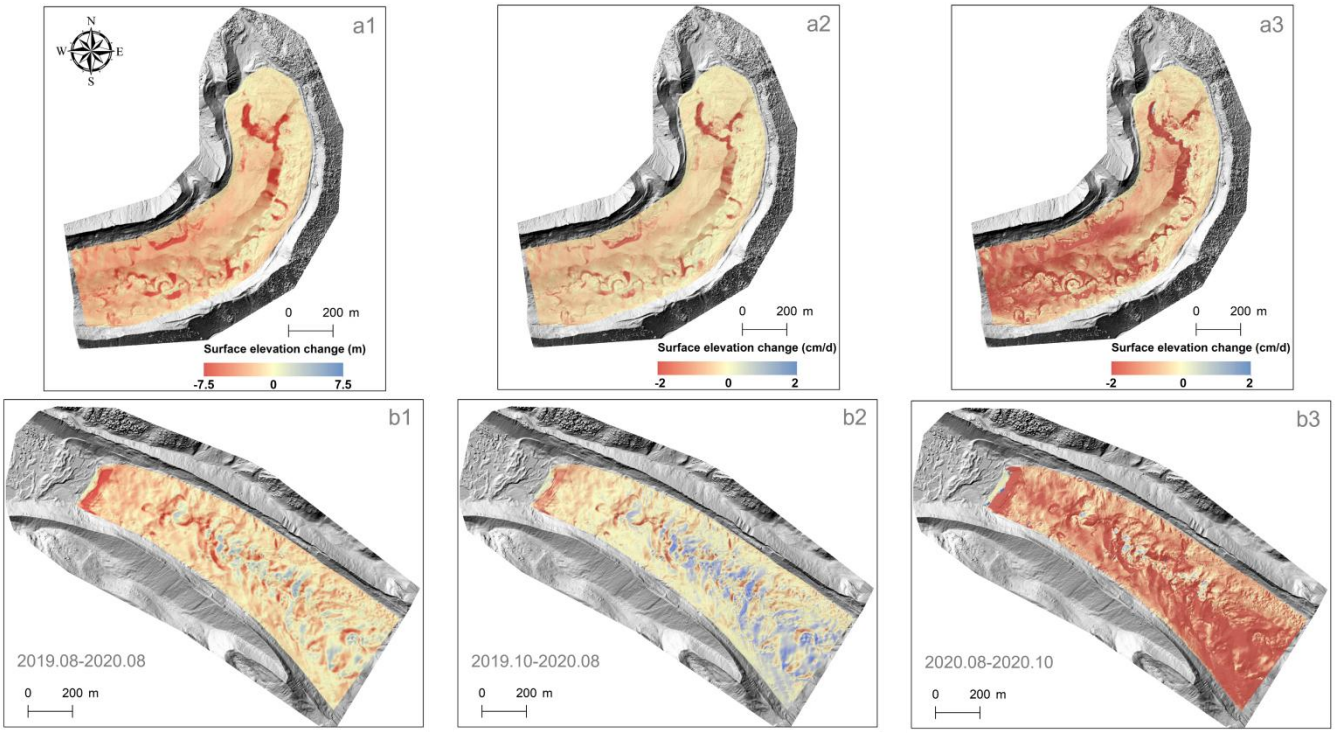

Figure 2: Annual surface elevation changes between UAV-derived DEMs for August 2019-August 2020 (a1, b1), the surface elevation change/thinning rates for the cold period (a2, b2) and the warm period (a3, b3). Upper panels refer to 23K Glacier and bottom panels refer to 24K Glacier.

255 In Figure.3, we present the relationships between thinning rates and altitude for each glacier at 5 m and 15 m intervals. The absolute thinning of 23K Glacier increases with altitude based on the Mann-Kendall test (i.e., a negative gradient; Z value: -3.75 - -3.25) for every analysis period, while the thinning of 24K Glacier decreases with altitude in the annual scale and cold period (positive gradient; Z value: +3.65 - +3.69). In particular, the thinning of 24K Glacier in the warm period shows the opposite altitudinal trend to its annual scale and cold period (i.e., consistent with 23K Glacier; Z value: -0.77).

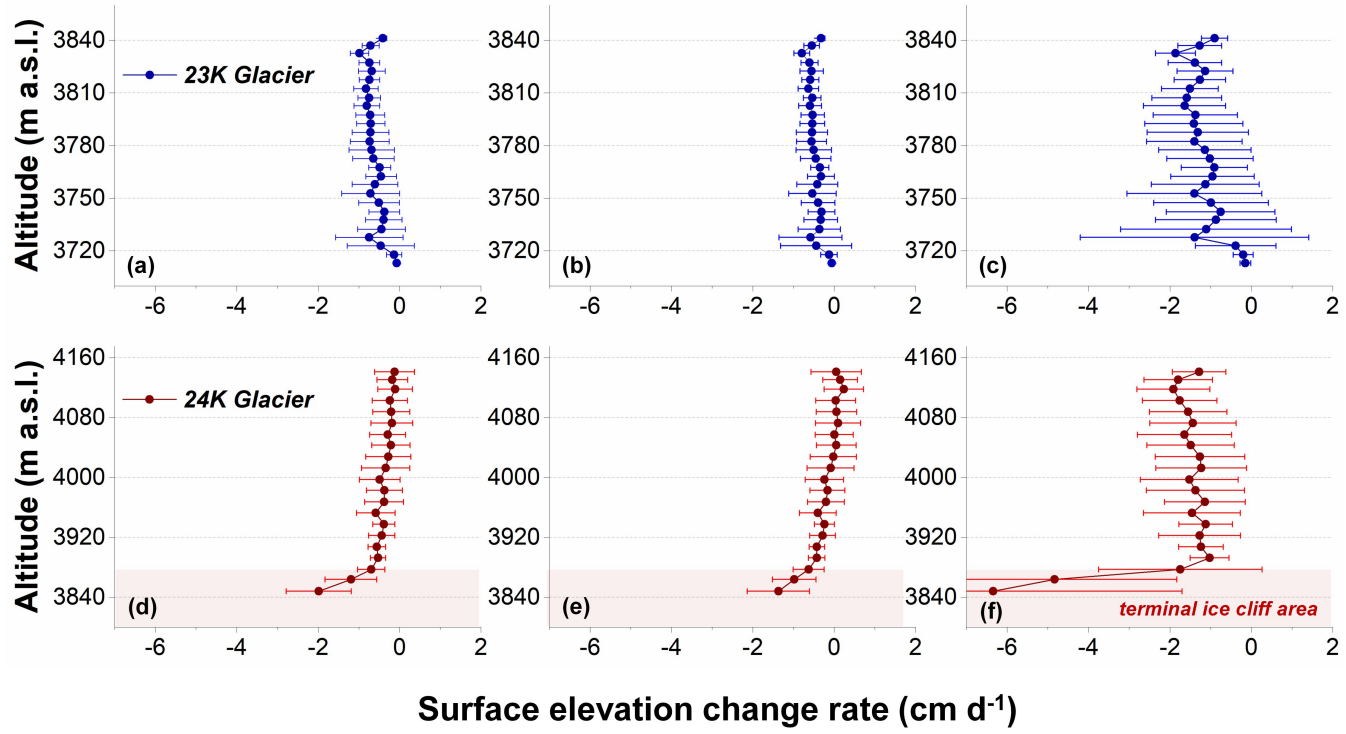

Figure 3: Annual average glacier surface elevation change rates within 5-m (23K Glacier)/15-m (24K) elevation bands (dots) with the corresponding standard deviations (horizontal error bar) for August 2019-August 2020 (a, d), the cold period (b, e) and the warm period (c, f) across the monitoring area of the two glaciers. The red shadowed sections represent the terminal ice cliff at of the 24K Glacier.

4.3 Glacier dynamics

Between August 2019 and August 2020, the mean surface velocity was 1.7 ± 0.2 m a^{-1} for 23K Glacier and 9.2 ± 0.2 m a^{-1} for 24K Glacier (Fig. 4a1, a2). There is a zone of stagnation at the terminus of 23K Glacier where the surface velocity is less than 2 m a^{-1} (from terminus to 900 m up-glacier, Fig. 4a1). During the cold period, the mean surface velocity of 23K Glacier was 0.4 ± 0.03 cm d^{-1}, while it was 2.4 ± 0.08 cm d^{-1} for 24K. During the warm period, the mean surface velocity for 23K Glacier and 24K Glacier was 0.6 ± 0.14 cm d^{-1} and 3.0 ± 0.40 cm d^{-1} respectively. For the UAV survey area, the mean driving stress of 23K Glacier was 1.6 × 10^5 Pa and for 24K Glacier was 2.1 × 10^5 Pa. The driving stress in the survey area for 24K Glacier was ~30% higher than for 23K Glacier (Fig. 4d). The estimated emergence velocities agreed with the insight from surface velocities and driving stress, with 24K Glacier having significantly higher emergence velocities than 23K Glacier at any period (Fig. 4e). ~~In this case,~~ the annual emergence of 23K (resp. 24K) Glacier was 0.18 ± 0.04 m (1.36 ± 0.14 m), and 24K Glacier was approximately 7.6 times higher than 23K Glacier. The mean emergence of cold period for 23K (resp. 24K) Glacier was 0.16 ± 0.03 m (1.14 ± 0.11 m), the warm period emergence velocity for 23K (resp. 24K)

Glacier was 0.07 ± 0.03 m (0.18 ± 0.04 m). 24K Glacier had consistently higher emergence velocity than 23K Glacier during all periods.

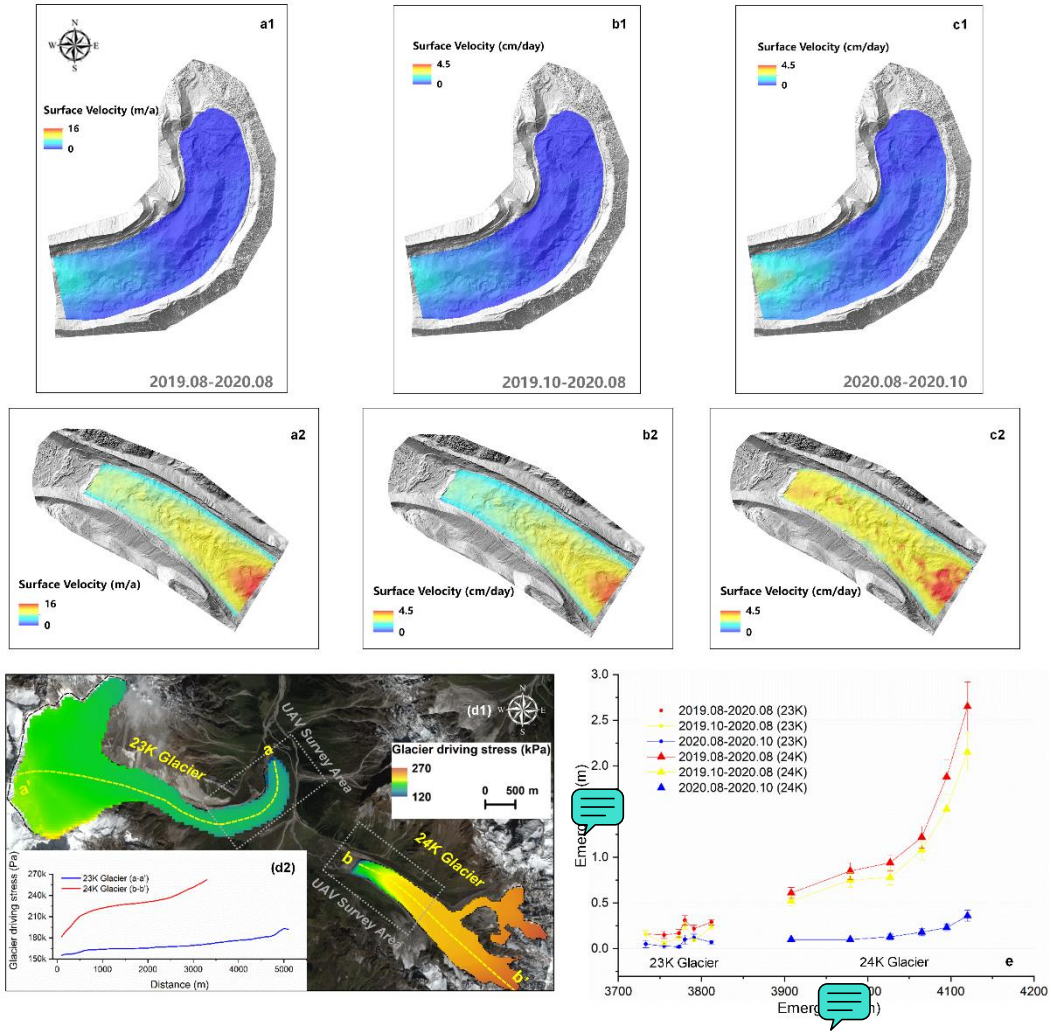

Figure 4: Average surface velocity for August 2019-August 2020 (a1, a2), the cold period (b1, b2) and the warm period (c1, c2). Spatial distribution of driving stresses (August 2019-August 2020) of the two glaciers (d1) and central flowlines (a-a' and b-b') driving stresses (d2), the grey dashed rectangular box (b1) represents the UAV aerial survey area, and we consider the confidence in the driving stress values of these parts to be higher than that of the upper part of the glacier, background image is a Pléiades-1A false-color image from 2021-09-20, which was used to derive the glacier outlines. © CNES 2021, Distribution Airbus D&S. The gradients between emergence velocity and altitude for two glaciers €.

4.4 Surface mass balance (SMB) patterns

At the annual scale, the mean surface mass balance for 23K and 24K Glacier survey areas were -2.5 ± 0.1 m w.e. a^{-1} and -2.8 ± 0.3 m w.e. a^{-1} respectively and are therefore not significantly different (Fig. 5). During the 'cold' period, the glacier mass balance was -0.5 ± 0.03 cm w.e. d^{-1} for 23K Glacier and -0.4 ± 0.09 cm w.e. d^{-1} for 24K Glacier (Fig. 5). In contrast, during the warm period, the mass balance of 23K Glacier was -1.3 ± 0.15 cm w.e. d^{-1}, while for 24K Glacier it was -1.9 ± 0.18 cm w.e. d^{-1}; the surface mass balance during the warm period for 24K Glacier is thus ~46% larger than for 23K Glacier (Fig. 5). The surface mass balance values of each mass balance zone (A-F) for both glaciers exhibit a weak decreasing trend with altitude in all periods (Fig. 7; Fig. S3).

To better evaluate the role of emergence velocity replenishment on thinning, we calculated the ratio of emergence velocity to surface mass balance (Table. 5). A higher absolute value of this ratio indicates a greater impact of emergence velocity replenishment on thinning ('-1' indicates perfect compensation of ablation by ice flow). The ratio of annual emergence velocity and annual surface mass balance for 23K (resp. 24K) Glacier is -0.09 (-0.49). The ratio of annual emergence velocity and annual surface mass balance for 23K and 24K Glacier are -0.09 and -0.49, respectively. The absolute ratio values for 24K Glacier are always higher than those for 23K Glacier, and this is especially evident in the non-ablation period.

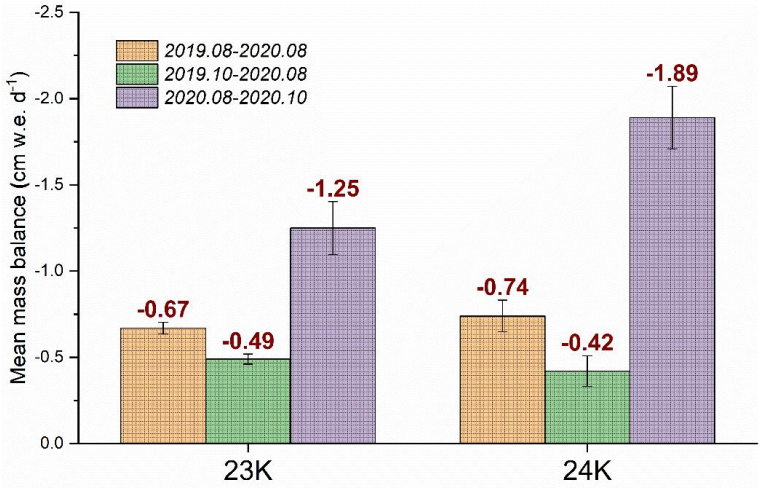

Figure 5: Mean surface mass balance rates and their uncertainties for both UAV survey domains during the annual observation period (2019.08-2020.08), the cold period (2019.10-2020.08) and the warm period (2020.08-2020.10).

Table 5: Emergence velocity, surface mass balance and the ratio of above two in all periods for both glaciers.

Time	Glacier	Emergence velocity (m w.e.)	Surface mass balance (m w.e.)	Ratio of emergence velocity to surface mass balance

Aug. 2019-Aug. 2020	23K	0.22 ± 0.04	-2.50 ± 0.11	-0.09
	24K	1.36 ± 0.14	-2.76 ± 0.34	-0.49
Oct. 2019-Aug. 2020	23K	0.16 ± 0.03	-1.53 ± 0.09	-0.11
	24K	1.14 ± 0.11	-1.31 ± 0.25	-0.87
Aug. 2020-Oct. 2020	23K	0.07 ± 0.03	-0.79 ± 0.09	-0.09
	24K	0.18 ± 0.04	-1.19 ± 0.11	-0.15

The density of ice cliffs and supraglacial ponds for 23K Glacier is 6.8-7.2% and is 4.4-5.1% for 24K Glacier (Table. 6). There are few ponds (~5, area > 100 m^2) on 23K Glacier, while there is no ponded area on 24K Glacier. The average debris thickness in the UAV survey area of 23K Glacier and 24K Glacier is 47.1 ± 2 cm and 24.2 ± 2 cm respectively. The debris thickness of both glaciers decreases with increasing altitude in the UAV survey area (23K Glacier: ~ -57 cm 100 m^{-1}; 24K Glacier: ~ -9 cm 100 m^{-1}). To disentangle the influence of the sub-debris area and the ice cliffs and supraglacial ponds area for the surface mass balance pattern respectively, we extracted the surface mass balance rates of the area of ice cliffs and supraglacial ponds and the sub-debris area in both glaciers for all periods (Table. 6). As shown in Table 6, the surface mass balance rates in the ice cliffs and supraglacial ponds area of both glaciers are higher than the sub-debris area during all periods (i.e., the ice cliffs and supraglacial ponds area possess the higher melt efficiency). In this study, the enhancement factors for the two glaciers range from 1.6 to 4.4 during all periods. The enhancement factors were consistently higher at 23K Glacier than at 24K Glacier (~1.5-1.8 times). They are significantly higher in the warm period than in the annual scale (23K: ~2.0 times； 24K: ~1.6 times) and the cold period (23K: ~1.7 times； 24K: ~1.5 times), indicating that the hotspots' effect is more pronounced during the ablation period. By extracting the ablation contribution of the ice cliffs and supraglacial ponds (Fig. 7), we found that the total melt from ice cliffs and supraglacial ponds areas accounted for 31.5 ± 2.2% of the total ablation in the UAV survey area for 23K Glacier and 11.4 ± 1.3% for 24K Glacier during the warm period.

Table 6: Ice cliffs and supraglacial ponds area proportion, mean ice cliffs and supraglacial ponds area and sub-debris area surface mass balance, ice cliffs and supraglacial ponds area enhancement factors in all periods for both glaciers.

Time	Glacier	Ice cliff and supraglacial pond area proportion (%)	Mean ice cliff and supraglacial pond area surface mass balance (cm w.e. d^{-1})	Mean sub-debris area surface mass balance (cm w.e. d^{-1})	Ice cliff and supraglacial pond area enhancement factors (-)
Aug. 2019-Aug. 2020	23K	6.8 ± 0.5	-1.3 ± 0.03	-0.6 ± 0.03	2.2
	24K	5.1 ± 0.5	-1.1 ± 0.1	-0.7 ± 0.1	1.6
Oct. 2019-Aug. 2020	23K	7.1 ± 0.5	-1.1 ± 0.03	-0.4 ± 0.03	2.6
	24K	4.9 ± 0.5	-0.7 ± 0.1	-0.4 ± 0.1	1.7
Aug. 2020-Oct. 2020	23K	7.2 ± 0.5	-4.1 ± 0.2	-0.9 ± 0.2	4.4
	24K	4.4 ± 0.5	-4.4 ± 0.2	-1.7 ± 0.2	2.6

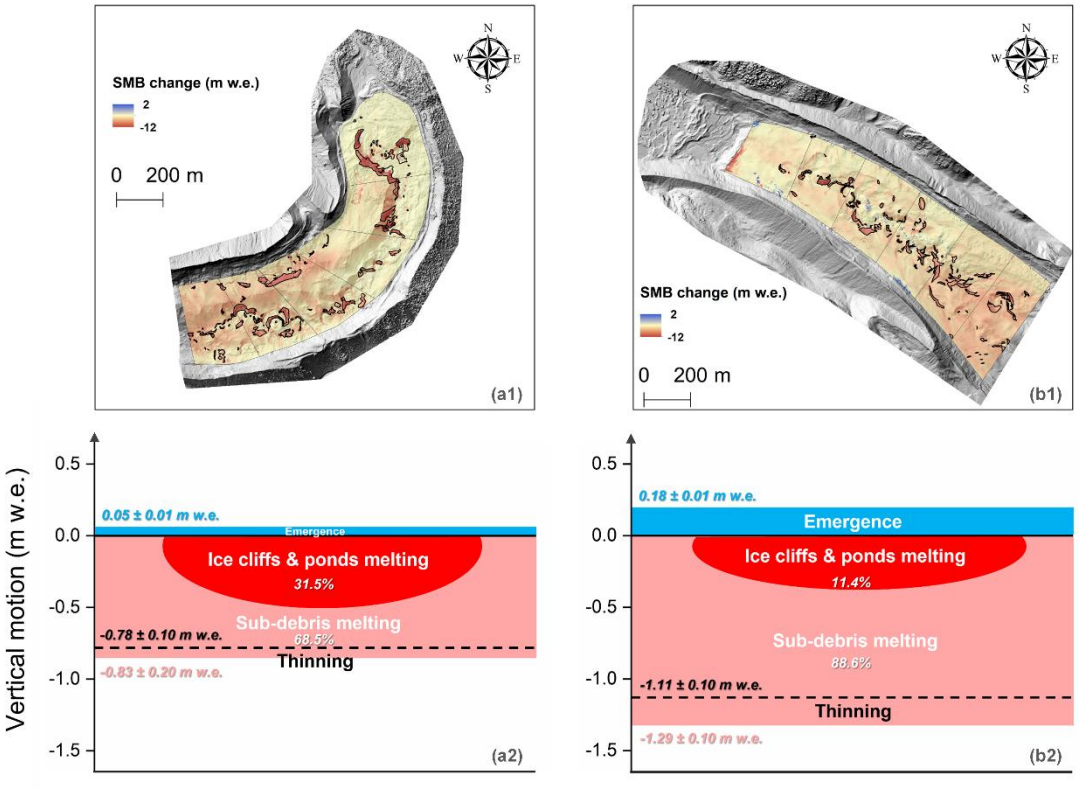

Figure 7: Spatial distribution of surface mass balance during the ablation period for the UAV survey domains of 23K Glacier and 24K Glacier (a1, b1). The a2 and b2 are the conceptual diagrams of vertical motion components for 23K Glacier and 24K Glacier.

To better disentangle the effects of debris thickness, and ice cliffs and supraglacial ponds on glacier melt, we compared the mean debris thickness, the percentage of ice cliff and supraglacial ponds and the mean melt rate during the warm period in each of the six zones (A-F) of each glacier (Fig. 8). We assessed the correlations between the zonal surface mass balance in the warm period and the zonal debris thickness and ice cliffs and supraglacial ponds density based on six points for each glacier. For 23K Glacier, the correlation coefficient *r*, between debris thickness and surface mass balance during the warm period is 0.88 (*p*-value = 0.02 at 95% confidence level), indicating that the debris thickness is highly correlated with the melt. In contrast, the correlation coefficient between the percentage of ice cliff and supraglacial ponds area, and the surface mass balance, is -0.29 (*p*-value = 0.58 at 95% confidence level), indicating the absence of a strong correlation. During the warm period, 24K Glacier also exhibits a strong relationship between the debris thickness and melt, with *r* is 0.82 (*p*-value = 0.05). The ice cliffs and supraglacial ponds area is weakly correlated with the glacier melt (*r* = -0.48, *p*-value = 0.36).

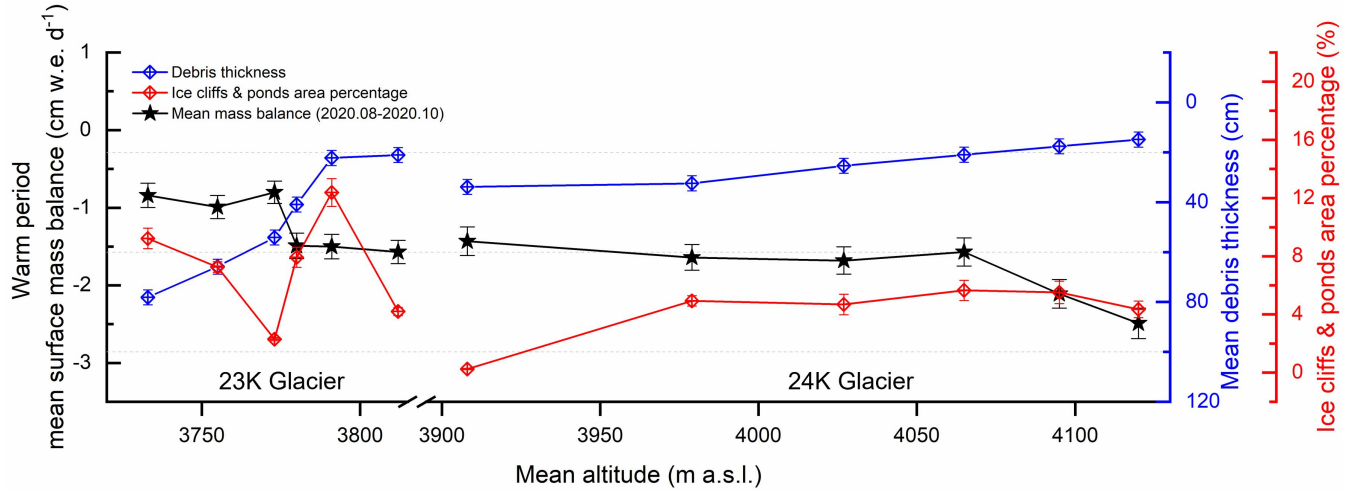

Figure 8: Daily surface mass balance during the warm period (black solid line), the mean debris thickness (blue solid line) and the mean percentage of the ice cliffs and supraglacial ponds area (red solid line) for the individual zones of two glaciers.

4.5 Glacier change in the early twenty-first century

The thinning of 23K Glacier tongue has been greater than that of 24K Glacier since 2000 (Hugonnet et al., 2021; Fig. 9), which is generally in agreement with the thinning patterns we derived from the UAV surveys. Both glaciers (UAV survey domains) show the inverted relationship of thinning against altitude at all periods of the last two decades. Both glaciers have experienced increases in thinning rates over this time period (increase rate for 23K: +77%; 24K: +100%), although the increase rate of 24K Glacier tongue is slightly lower than that of 23K Glacier over the last decade (23K: +44%; 24K: +20%).

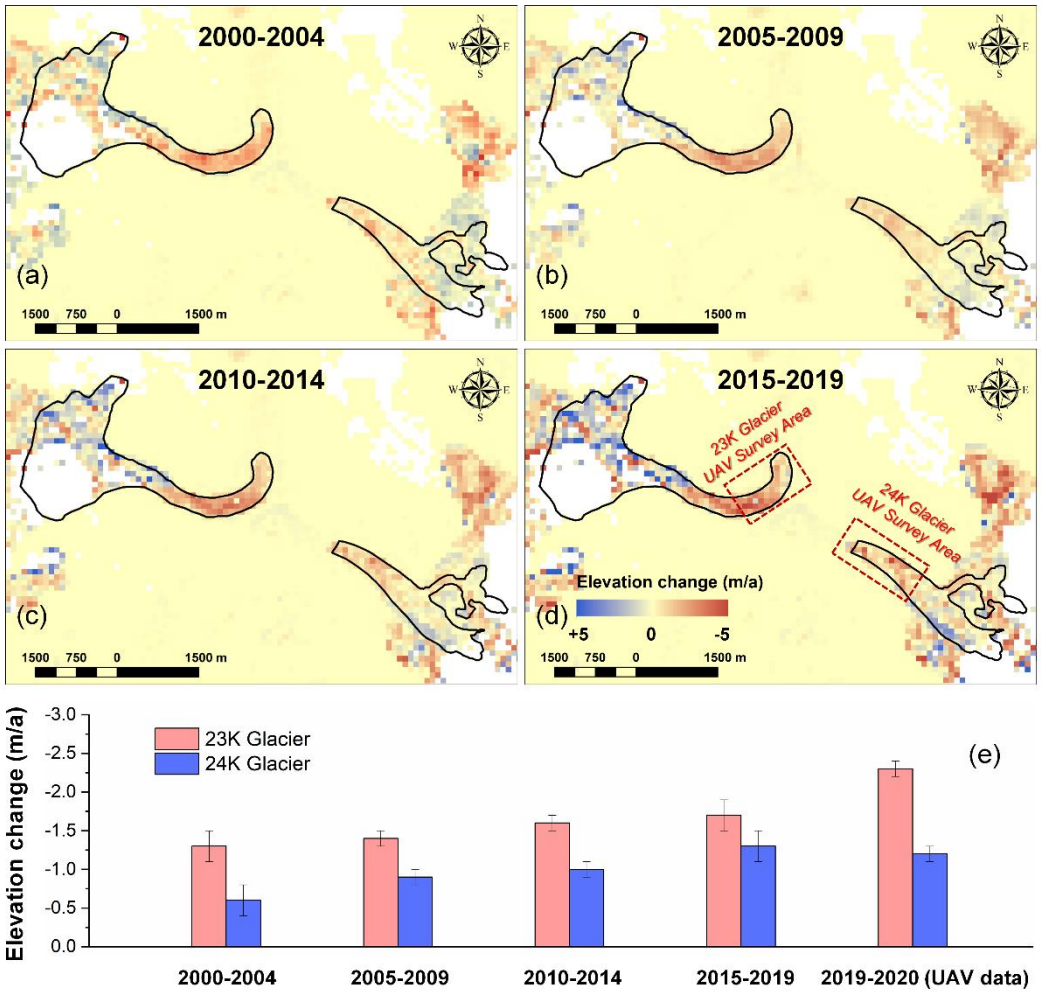

Figure 9: Annual surface elevation changes for 2000-2004 (a), 2005-2009 (b), 2010-2014 (c), 2015-2019(d) for the 23K Glacier and 24K Glacier (red dashed rectangular box represents the UAV aerial survey area). Annual surface elevation changes and their uncertainties for both UAV survey domains at different periods (e).

Combined with our work and Dehecq et al (2015), we explore changes in the glaciers' dynamic state by analysing the surface velocities over the last two decades (Fig. 10). It is found that the surface velocities of both glaciers (UAV survey domains) decreased significantly in the first fifteen years of this century with the surface velocities of 1999-2003 and 2013-2015. During this period, the surface velocity of 23K and 24K Glaciers decreased on average by 84% and 54% respectively. However, the velocity magnitude and pattern for 2013-2015 corresponds to our UAV results. The 24K Glacier tongue is still replenished by ice flux at present, which compensates for its higher melt due to thinner debris. We expect ice supply to continue to deteriorate as these glaciers thin (Dehecq et al., 2019) and it is necessary to carry out high-precision surface velocity observations to understand these glaciers' future fate.

A prior study analyzed the mean surface mass balance for the survey domains from 2000-2016 based on regionally-available datasets (Miles et al., 2021), estimating -1.5 ± 0.7 m w.e. a^{-1} (23K) and -1.6 ± 1.1 m w.e. a^{-1} (24K). These values are lower than our ratess for 2019-2020, which might be attributed to warming or to changes in precipitation timing in the Southeast Tibetan Plateau (e.g., Jouberton et al., 2022). For 2000-2016, the magnitude of surface mass balance was slightly greater on 24K Glacier than on 23K Glacier, which is consistent with our surface mass balance results for 2019-2020 derived from the UAV data.

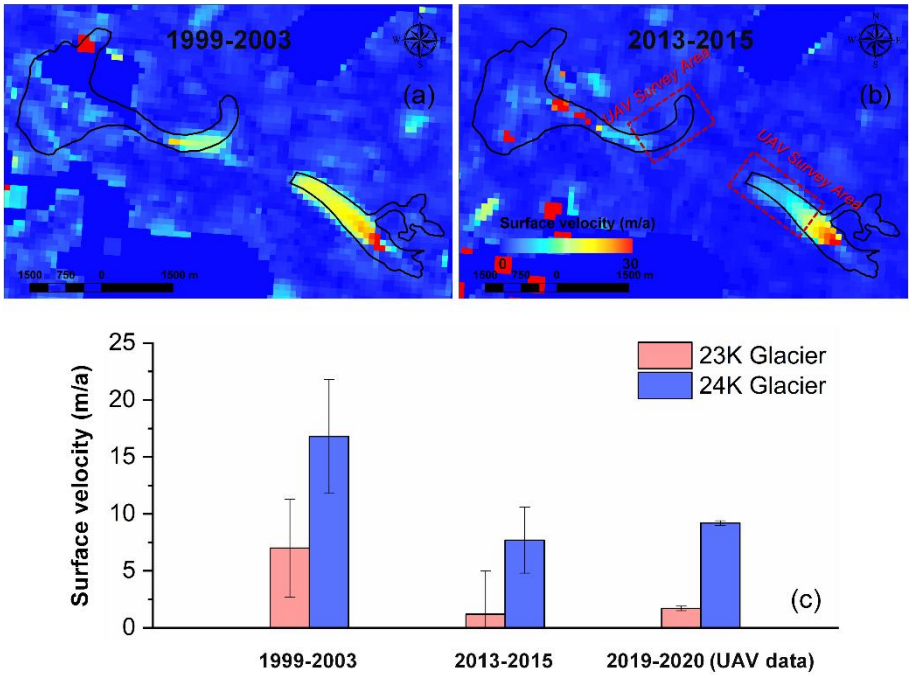

Figure 10: Annual surface velocity for 1999-2003 (a), 2013-2015 (b) for the 23K Glacier and 24K Glacier (red dashed rectangular box represents the UAV aerial survey area). Annual surface velocities and their uncertainties for both UAV survey domains at different periods (c).

5 Discussion

5.1 Controls on the thinning (d*h*) patterns

The thinning patterns of the two glaciers are different at the annual scale and during the cold period, as indicated by their magnitude and spatial distribution (Fig.2). The annual thinning rate of 23K Glacier is approximately twice that of 24K Glacier, but the rate at which surface mass balance evolves with altitude exhibits less variation between the two glaciers (Fig. 6, Figure S3). Some studies have highlighted that large differences in thinning can be caused by different dynamic states (Fig. 4; Brun et al., 2018; Anderson et al., 2021a, 2021b; Rounce et al., 2021). In this study, the emergence velocity replenishment is consistently higher on 24K Glacier than on 23K Glacier for all periods (Fig. 4e) (Fig. 4a-d). The replenishment of ice into

the ablation area by ice flow is crucial to the glaciers' long-term sustainability, and net annual ablation exceeds ice resupply for the study areas of both glaciers. We therefore assess the ratio of emergence velocity to surface mass balance as an indicator of the local balance between ablation and ice supply (a direct local metric of glacier health), and this study illustrates that glacier health can vary greatly even over small distances (Table 5). 23K and 24K Glaciers experience the same climatic forcing, but their distinct geometries lead to different expressions of ice dynamics. For instance, the mean longitudinal gradient of 24K Glacier (~0.18) is consistently higher than that of 23K Glacier (~0.08), which explains the higher driving stress (Fig. S8) and, consequently, faster surface velocity of 24K Glacier. In addition, the different glacier geometries may lead to distinct dependence on avalanche and rockfall mass supply, which could also lead to marked differences in mass supply to the glacier terminus. Using the ratio of emergence to surface mass balance, we can identify, for each season, whether ice resupply or surface mass balance is the main factor leading to the thinning rates. In Table 5, we clearly see that at 23K Glacier, ice supply is considerably smaller (-0.11) than surface mass balance for all periods, indicating that surface mass balance is directly responsible for contemporary thinning patterns. 24K Glacier also exhibits a strong imbalance between ice emergence and surface mass balance over the warm period (-0.15), but emergence nearly compensates for surface mass balance during the cold period (-0.87). Thus, 24K Glacier exhibits a healthier cold-season and annual balance between ablation and ice supply than 23K Glacier. In contrast to the annual and cold period, the thinning patterns of the two glaciers are similar during the warm period (i.e., the magnitude of thinning increases with altitude). In this period, the 24K Glacier emergence velocity only represents a small fraction of the melt (Table 5), and the pattern of surface mass balance is clearly driven by the spatial distribution of debris thickness. Therefore, during the warm period, the thinning pattern of 24K Glacier goes from being controlled primarily by ice dynamics (for the annual and cold period) to being controlled by debris thickness.

Fu et al. (2022) also estimated thinning for a debris-covered glacier (Hailuogou) in the southeastern Tibetan Plateau. They revealed that the tongue area showed a considerable thinning (-2.81 m) during an ablation period (June. 2018-Oct. 2018) and that its ice resupply is very weak, similar to what we observe for 23K Glacier. He et al. (2023) have also observed the tongue area of a debris-covered glacier (Zhuxi) in the southeastern Tibetan Plateau by UAV from 2020-2021. The lower tongue of this glacier is similarly characterised by high rates of thinning (>1 m a^{-1}) and slow movement (< 7 m a^{-1}). Other studies concerning the mass balance of Himalayan debris-covered glaciers also report on glaciers which possess a high thinning rate (~-0.9-1.8 m a^{-1}) and weaker dynamic state (Vincent et al., 2016; Nuimura et al., 2017; Brun et al., 2018; Rowan et al., 2021), and which possess thinning patterns which are consistent with that of 23K Glacier. In summary, the thinning pattern for 23K Glacier appears to conform to that of other Himalayan debris-covered glaciers, whilst that of 24K Glacier is perhaps more anomalous due to its relatively healthy ice supply all the way to the terminus.

In-situ observations show that the terminus type differs between each glacier (Fig. 1c, 1d, Fig. S4), which can have a strong influence on ice dynamics for debris-covered glaciers (Anderson and Anderson, 2016). The terminus of 23K Glacier appears

largely stagnant and is enclosed by a latero-terminal moraine complex, while the terminus of 24K Glacier exhibits a large ice cliff bounded by lateral moraines. The mass of 24K Glacier is lost due to progressive melt, and episodic 'dry' calving promotes glacier retreat. Such terminal-cliff debris-covered glaciers are less well studied but have been noted in a variety of settings (e.g., Ferguson and Vieli, 2021). Terminus type can have an important influence on debris-covered glacier geometry (King et al., 2019) and may thus influence glacier geometric evolution in a warming climate. Our investigations suggest that 24K Glacier exhibits reduced climatic-geometric imbalance than 23K Glacier, possibly because it has responded to climate warming with progressive retreat, rather than thinning. In addition, the ablation area of 23K Glacier is largely stagnant with a low thinning rate (> -0.5 m a^{-1}) and the lower mean surface velocities and reduced driving stress, which favor the presence of supraglacial ponds that enable the persistence of relatively large pond-influenced cliffs (Quincey et al., 2007; Sakai and Fujita, 2010; Miles et al., 2017; Kneib et al., 2023). On the contrary, due to a steeper longitudinal gradient and stronger ice flux, 24K Glacier is characterized by thinner debris which, combined with the steeper gradient, allows for the development of supraglacial streams and corresponding stream-influenced cliffs (Mölg et al., 2020; Kneib et al., 2023).

5.2 Possible reasons for surface mass balance (SMB) patterns

The presence of a debris cover and its influence on ablation typically causes surface mass balance patterns for debris-covered glaciers to differ from those of largely debris-free glaciers due to the melt-buffering effect of supraglacial debris cover that exceeds a few centimeters in thickness (Ostrem, 1959; Nakawo et al., 1999; Nicholson and Benn, 2006; Reid and Brock, 2010; Anderson and Anderson, 2016; Yang et al., 2017). Our results show inverted melt-season surface mass balance profiles for both 23K and 24K Glaciers. In addition, debris-covered glaciers tend to develop ice cliffs which enhance melt locally, even relative to clean ice (Sakai, 1998, 2002; Reid and Brock, 2014; Juen et al., 2014; Steiner et al., 2015; Buri et al., 2016, 2021; Miles et al., 2016, 2018, 2022; Kneib et al., 2022). Overall, the annual surface mass balance of 23K Glacier and 24K Glacier are similar, but the rate of mass loss is higher for 24K Glacier during the warm period due to its thinner debris cover. During all periods, the magnitude of ablation increases with elevation for both glaciers, with the same spatial distribution (Fig. 8, Fig. S3). We find that the correlation between the melt and the debris thickness distribution is strong for both glaciers (23K: r=0.88; 24K: r=0.82) during the warm period, while there is little correlation between the melt and the ice cliffs and supraglacial ponds area distribution (23K: r=-0.29; 24K: r=-0.48). Prior studies have also identified the effect of the debris thickness spatial distribution on the physical mechanisms of ablation (Mihalcea et al., 2008; Zhang et al., 2011; Reid et al., 2012; Juen et al., 2014; Zhang et al., 2016; Gibson et al., 2017; McCarthy et al., 2017).

With the relationship between surface mass balance and debris thickness established for the two glaciers during the ablation period, we found that the mean residuals sourced from surface mass balance-debris thickness relationship of 23K Glacier were larger than the 24K Glacier (47.1 *vs* 24.2). Although there is no direct correlation between surface mass balance and ice cliffs and supraglacial ponds, the above nearly double residual difference is hypothesized to be based on the large difference in ice cliffs and supraglacial ponds area enhancement factors of two glaciers (23K: 4.4, 24K: 2.6; ~1.7 times), and reflects

some of the influence of ice cliffs and supraglacial ponds area on surface mass balance/melt pattens. Based on UAV and time-lapse camera observations, Kneib et al. (2022) carried out high-precision observation of a single ice cliff on 24K Glacier, and measured the daily cliff melt during the ablation period at 3.9-5.1 cm day^{-1}. In this study, the daily melt of the 24K Glacier ice cliffs and supraglacial ponds areas during the warm period was estimated to be 4.4 ± 0.2 cm w.e. d^{-1} (~4.9 cm day^{-1}), which is similar to the observed value for a single ice cliff. The role of ice cliffs and supraglacial ponds area is not negligible, as ablation in the survey areas would be underestimated by 24.5 ± 1.7% (23K) and 7.0 ± 0.7% (24K), respectively, if the ice cliffs and supraglacial ponds areas were not taken into account. Other studies have observed and simulated the contribution of ice cliffs to be 17-26% of the total ablation, which is in agreement with our results (Brun et al., 2018; Anderson et al., 2021a; Buri et al., 2021). However, the areal proportion of ice cliffs and supraglacial ponds areas (23K Glacier: 7.2 ± 0.5 %, 24K Glacier: 4.4 ± 0.5 %) is much smaller than that of the sub-debris melt area for each glacier. This has the overall effect that enhanced melt in these regions does not have a marked effect on glacier-scale surface mass balance profiles, but rather leads to an increase in ablation throughout the debris-covered area. We note that in this study the outlines of ice cliffs and supraglacial ponds area as digitized for warm periods were based on the merged outlines (Brun et al., 2018), which may lead to an overestimation of the extent of the ice cliffs and supraglacial ponds area (Kneib et al., 2022). While the ice cliffs and supraglacial ponds are local controls of melt patterns, debris thickness is the dominant control on the altitudinal surface mass balance pattern for both 23K and 24K Glaciers, similar to the at Kennicott Glacier in Alaska (Anderson et al, 2021a).

This study gives us insight into the controlling role of the debris thickness on ablation patterns of debris-covered glaciers. In future research, it will be beneficial to improve our understanding of the responses of debris-covered glaciers to climate change by focusing on the debris supply and evacuation differences. Based on field photography (Fig. S5), we also found that paraglacial slope failure events have occurred in the catchment of 23K Glacier recently and may be the result of complex interactions between geologic structure and stress-related slope response to glacier mass loss (Zhong et al., 2022). Such events may become an increasingly important component of the debris supply and transport cascade for these land systems, with implications for the future development of supraglacial debris cover, glacier mass balance, and flow dynamics; large rock avalanches which emplace in supraglacial environments have led to melt suppression and glacier advance in other locations (e.g., McSaveney, 1975; Shugar and Clague, 2011), and, if sufficiently thick, this event could thus temporarily rejuvenate the emergence velocity into the terminus area.

Conclusions

We have used multi-temporal high-resolution UAV-SfM surveys combined with *in-situ* observations to quantify seasonal thinning (d*h*) and surface mass balance (SMB) of two neighboring, but contrasting, debris-covered glaciers in the southeastern Tibetan Plateau. The conclusions are summarized as follows：

1) The thinning (d*h*) patterns of the two glaciers display distinct characteristics at annual scale. The annual thinning of 23K Glacier UAV survey area is 1.9 times greater than that of 24K Glacier. The magnitude of 23K Glacier thinning increases with altitude, similar to many other debris-covered glaciers, whereas 24K Glacier shows the opposite pattern, except during the melt season. These contrasting patterns are mainly driven by the stronger dynamic state of 24K Glacier, which has a much higher down valley emergence velocity replenishment. However, the thinning pattern of 24K Glacier is similar with that of 23K Glacier during the warm period (i.e., the magnitude of thinning increases with altitude). In this period, the thinning of 24K Glacier is mainly controlled by melt.

2) The surface mass balance (SMB) patterns of the two glaciers are generally in agreement. The magnitude of surface mass balance on both glaciers increases with altitude in the ablation period, exhibiting melt inversion which is attributable to the debris thickness distribution (which decreases with altitude). Due to the low areal proportion of ice cliffs and supraglacial ponds area (melt hotspots), sub-debris ablation accounts for the majority of the total ablation.

3) Both glaciers experience accelerated thinning and reduced flow in their ablation area. 23K Glacier possesses the higher thinning rate and is in a weaker dynamic state than 24K Glacier, a pattern that is confirmed on the longer term.

4) High-resolution and comparative observation gives a rare perspective into the controls of the thinning and melt of two debris-covered glaciers. We provide evidence that the rate of mass loss on such glaciers can be highly dependent on dynamic state, and that the relatively thin debris on these glaciers is the main control of the glacier surface ablation patterns, with supraglacial cliffs and ponds primarily serving to enhance mass loss.

References

Allen, S. K., Zhang, G. Q., Wang, W. C., Yao, T. D., and Bolch, T.: Potentially dangerous glacial lakes across the Tibetan Plateau revealed using a large-scale automated assessment approach, Science Bulletin, 64, 435-445, 10.1016/j.scib.2019.03.011, 2019.

An, B. S., Wang, W. C., Yang, W., Wu, G. J., Guo, Y. H., Zhu, H. F., Gao, Y., Bai, L., Zhang, F., Zeng, C., Wang, L., Zhou, J., Li, X., Li, J., Zhao, Z. J., Chen, Y. Y., Liu, J. S., Li, J. L., Wang, Z. Y., Chen, W. F., and Yao, T. D.: Process, mechanisms, and early warning of glacier collapse-induced river blocking disasters in the Yarlung Tsangpo Grand Canyon, southeastern Tibetan Plateau, Science of the Total Environment, 816, 10.1016/j.scitotenv.2021.151652, 2022.

Anderson, L. S. and Anderson, R. S.: Modeling debris-covered glaciers: response to steady debris deposition, Cryosphere, 10, 1105-1124, 10.5194/tc-10-1105-2016, 2016.

Anderson, L. S. and Anderson, R. S.: Debris thickness patterns on debris-covered glaciers, Geomorphology, 311, 1-12, 10.1016/j.geomorph.2018.03.014, 2018.

Anderson, L. S., Armstrong, W. H., Anderson, R. S., and Buri, P.: Debris cover and the thinning of Kennicott Glacier, Alaska: in situ measurements, automated ice cliff delineation and distributed melt estimates, Cryosphere, 15, 265-282, 10.5194/tc-15-265-2021, 2021a.

Anderson, L. S., Armstrong, W. H., Anderson, R. S., Scherler, D., and Petersen, E.: The causes of debris-covered glacier thinning: evidence for the importance of ice dynamics from Kennicott Glacier, Alaska, Frontiers in Earth Science, 9, 10.3389/feart.2021.680995, 2021b.

Bash, E. A. and Moorman, B. J.: Surface melt and the importance of water flow - an analysis based on high-resolution unmanned aerial vehicle (UAV) data for an Arctic glacier, Cryosphere, 14, 549-563, 10.5194/tc-14-549-2020, 2020.

Benn, D. I., Bolch, T., Hands, K., Gulley, J., Luckman, A., Nicholson, L. I., Quincey, D., Thompson, S., Toumi, R., and Wiseman, S.: Response of debris-covered glaciers in the Mount Everest region to recent warming, and implications for outburst flood hazards, Earth-Science Reviews, 114, 156-174, 10.1016/j.earscirev.2012.03.008, 2012.

Benoit, L., Gourdon, A., Vallat, R., Irarrazaval, I., Gravey, M., Lehmann, B., Prasicek, G., Graff, D., Herman, F., and Mariethoz, G.: A high-resolution image time series of the Gorner Glacier - Swiss Alps - derived from repeated unmanned aerial vehicle surveys, Earth System Science Data, 11, 579-588, 10.5194/essd-11-579-2019, 2019.

Bolch, T., Menounos, B., and Wheate, R.: Landsat-based inventory of glaciers in western Canada, 1985–2005, Remote Sens. Environ., 114, 127–137, https://doi.org/10.1016/j.rse.2009.08.015, 2010.

Brun, F., Berthier, E., Wagnon, P., Kaab, A., and Treichler, D.: A spatially resolved estimate of High Mountain Asia glacier mass balances from 2000 to 2016, Nature Geoscience, 10, 668-+, 10.1038/ngeo2999, 2017.

Brun, F., Buri, P., Miles, E. S., Wagnon, P., Steiner, J., Berthier, E., Ragettli, S., Kraaijenbrink, P., Immerzeel, W. W., and Pellicciotti, F.: Quantifying volume loss from ice cliffs on debris-covered glaciers using high-resolution terrestrial and aerial photogrammetry, Journal of Glaciology, 62, 684-695, 10.1017/jog.2016.54, 2016.

Brun, F., Wagnon, P., Berthier, E., Shea, J. M., Immerzeel, W. W., Kraaijenbrink, P. D. A., Vincent, C., Reverchon, C., Shrestha, D., and Arnaud, Y.: Ice cliff contribution to the tongue-wide ablation of Changri Nup Glacier, Nepal, central Himalaya, Cryosphere, 12, 3439-3457, 10.5194/tc-12-3439-2018, 2018.

Brun, F., Wagnon, P., Berthier, E., Jomelli, V., Maharjan, S. B., Shrestha, F., and Kraaijenbrink, P. D. A.: Heterogeneous Influence of Glacier Morphology on the Mass Balance Variability in High Mountain Asia, Journal of Geophysical Research-Earth Surface, 124, 1331-1345, 10.1029/2018jf004838, 2019.

Buri, P., Miles, E. S., Steiner, J. F., Immerzeel, W. W., Wagnon, P., and Pellicciotti, F.: A physically based 3-D model of ice cliff evolution over debris-covered glaciers, Journal of Geophysical Research-Earth Surface, 121, 2471-2493, 10.1002/2016jf004039, 2016.

Buri, P., Miles, E. S., Steiner, J. F., Ragettli, S., and Pellicciotti, F.: Supraglacial Ice Cliffs Can Substantially Increase the Mass Loss of Debris-Covered Glaciers, Geophysical Research Letters, 48, 10.1029/2020gl092150, 2021.

Cao, B., Guan, W. J., Li, K. J., Pan, B. T., and Sun, X. D.: High-Resolution Monitoring of Glacier Mass Balance and Dynamics with Unmanned Aerial Vehicles on the Ningchan No. 1 Glacier in the Qilian Mountains, China, Remote Sensing, 13, 10.3390/rs13142735, 2021.

Cuffey, K. M. and Paterson, W. S. B.: The Physics of Glaciers, Fourth Edition, Academic Press, Amsterdam, 704 pp., 2010.

Dehecq, A., Gourmelen, N., and Trouve, E.: Deriving large-scale glacier velocities from a complete satellite archive: Application to the Pamir-Karakoram-Himalaya, Remote Sensing of Environment, 162, 55-66, 10.1016/j.rse.2015.01.031, 2015.

Dehecq, A., Gourmelen, N., Gardner, A. S., Brun, F., Goldberg, D., Nienow, P. W., Berthier, E., Vincent, C., Wagnon, P., and Trouve, E.: Twenty-first century glacier slowdown driven by mass loss in High Mountain Asia, Nature Geoscience, 12, 22-+, 10.1038/s41561-018-0271-9, 2019.

Farinotti, D., Huss, M., Furst, J. J., Landmann, J., Machguth, H., Maussion, F., and Pandit, A.: A consensus estimate for the ice thickness distribution of all glaciers on Earth, Nature Geoscience, 12, 168-+, 10.1038/s41561-019-0300-3, 2019.

Ferguson, J. C. and Vieli, A.: Modelling steady states and the transient response of debris-covered glaciers, Cryosphere, 15, 3377-3399, 10.5194/tc-15-3377-2021, 2021.

Fu, Y., Liu, Q., Liu, G. X., Zhang, B., Zhang, R., Cai, J. L., Wang, X. W., and Xiang, W.: Seasonal ice dynamics in the lower ablation zone of Dagongba Glacier, southeastern Tibetan Plateau, from multitemporal UAV images, Journal of Glaciology, 10.1017/jog.2021.123, 2022.

Fugazza, D., Scaioni, M., Corti, M., D'Agata, C., Azzoni, R. S., Cernuschi, M., Smiraglia, C., and Diolaiuti, G. A.: Combination of UAV and terrestrial photogrammetry to assess rapid glacier evolution and map glacier hazards, Natural Hazards and Earth System Sciences, 18, 1055-1071, 10.5194/nhess-18-1055-2018, 2018.

Fugger, S., Fyffe, C. L., Fatichi, S., Miles, E., McCarthy, M., Shaw, T. E., Ding, B. H., Yang, W., Wagnon, P., Immerzeel, W., Liu, Q., and Pellicciotti, F.: Understanding monsoon controls on the energy and mass balance of glaciers in the Central and Eastern Himalaya, Cryosphere, 16, 1631-1652, 10.5194/tc-16-1631-2022, 2022.

Fujita, K. and Ageta, Y.: Effect of summer accumulation on glacier mass balance on the Tibetan Plateau revealed by mass-balance model, Journal of Glaciology, 46, 244-252, 10.3189/172756500781832945, 2000.

Gardelle, J., Berthier, E., Arnaud, Y., and Kaab, A.: Region-wide glacier mass balances over the Pamir-Karakoram-Himalaya during 1999-2011, Cryosphere, 7, 1263-1286, 10.5194/tc-7-1263-2013, 2013.

Gibson, M. J., Glasser, N. F., Quincey, D. J., Mayer, C., Rowan, A. V., and Irvine-Fynn, T. D. L.: Temporal variations in supraglacial debris distribution on Baltoro Glacier, Karakoram between 2001 and 2012, Geomorphology, 295, 572-585, 10.1016/j.geomorph.2017.08.012, 2017.

Hambrey, M. J., Quincey, D. J., Glasser, N. F., Reynolds, J. M., Richardson, S. J., and Clemmens, S.: Sedimentological, geomorphological and dynamic context of debris-mantled glaciers, Mount Everest (Sagarmatha) region, Nepal, Quaternary Science Reviews, 27, 2361-2389, 10.1016/j.quascirev.2008.08.010, 2008.

Herreid, S. and Pellicciotti, F.: The state of rock debris covering Earth's glaciers, Nature Geoscience, 13, 621, 10.1038/s41561-020-0615-0, 2020.

He, Z., Yang, W., Wang, Y. J., Zhao, C. X., Ren, S. T., and Li, C. H.: Dynamic Changes of a Thick Debris-Covered Glacier in the Southeastern Tibetan Plateau, Remote Sensing, 15, 10.3390/rs15020357, 2023.

Hugenholtz, C. H., Whitehead, K., Brown, O. W., Barchyn, T. E., Moorman, B. J., LeClair, A., Riddell, K., and Hamilton, T.: Geomorphological mapping with a small unmanned aircraft system (sUAS): Feature detection and accuracy assessment of a photogrammetrically-derived digital terrain model, Geomorphology, 194, 16-24, 10.1016/j.geomorph.2013.03.023, 2013.

Hugonnet, R., McNabb, R., Berthier, E., Menounos, B., Nuth, C., Girod, L., Farinotti, D., Huss, M., Dussaillant, I., Brun, F., and Kaab, A.: Accelerated global glacier mass loss in the early twenty-first century, Nature, 592, 726-+, 10.1038/s41586-021-03436, 2021.

Immerzeel, W. W., Kraaijenbrink, P. D. A., Shea, J. M., Shrestha, A. B., Pellicciotti, F., Bierkens, M. F. P., and de Jong, S. M.: High-resolution monitoring of Himalayan glacier dynamics using unmanned aerial vehicles, Remote Sensing of Environment, 150, 93-103, 10.1016/j.rse.2014.04.025, 2014.

James, M. R., Robson, S., and Smith, M. W.: 3-D uncertainty-based topographic change detection with structure-from-motion photogrammetry: precision maps for ground control and directly georeferenced surveys, Earth Surface Processes and Landforms, 42, 1769-1788, 10.1002/esp.4125, 2017.

Jouberton, A., Shaw, T. E., Miles, E., McCarthy, M., Fugger, S., Ren, S. T., Dehecq, A., Yang, W., and Pellicciotti, F.: Warming-induced monsoon precipitation phase change intensifies glacier mass loss in the southeastern Tibetan Plateau, Proceedings of the National Academy of Sciences of the United States of America, 119, 10.1073/pnas.2109796119, 2022.

Juen, M., Mayer, C., Lambrecht, A., Han, H., and Liu, S.: Impact of varying debris cover thickness on ablation: a case study for Koxkar Glacier in the Tien Shan, Cryosphere, 8, 377-386, 10.5194/tc-8-377-2014, 2014.

Kaab, A., Berthier, E., Nuth, C., Gardelle, J., and Arnaud, Y.: Contrasting patterns of early twenty-first-century glacier mass change in the Himalayas, Nature, 488, 495-498, 10.1038/nature11324, 2012.

Kaab, A., Jacquemart, M., Gilbert, A., Leinss, S., Girod, L., Huggel, C., Falaschi, D., Ugalde, F., Petrakov, D., Chernomorets, S., Dokukin, M., Paul, F., Gascoin, S., Berthier, E., and Kargel, J. S.: Sudden large-volume detachments of low-angle mountain glaciers more frequent than thought?, Cryosphere, 15, 1751-1785, 10.5194/tc-15-1751-2021, 2021.

Kaab, A., Kaufmann, V., Ladstadter, R., and Eiken, T.: Rock glacier dynamics: implications from high-resolution measurements of surface velocity fields, 8th International Conference on Permafrost, Zurich, Switzerland, Jul 21-25, WOS:000185049300089, 501-506, 2003.

Ke, L. H., Song, C. Q., Yong, B., Lei, Y. B., and Ding, X. L.: Which heterogeneous glacier melting patterns can be robustly observed from space? A multi-scale assessment in southeastern Tibetan Plateau, Remote Sensing of Environment, 242, 10.1016/j.rse.2020.111777, 2020.

Kneib, M., Miles, E. S., Buri, P., Molnar, P., McCarthy, M., Fugger, S., and Pellicciotti, F.: Interannual Dynamics of Ice Cliff Populations on Debris-Covered Glaciers From Remote Sensing Observations and Stochastic Modeling, Journal of Geophysical Research-Earth Surface, 126, 10.1029/2021jf006179, 2021.

Kneib, M., Miles, E.S., Buri, P., Fugger, S., McCarthy, M., Shaw, T.E., Chuanxi, Z., Truffer, M., Westoby, M.J., Yang, W. and Pellicciotti, F.: Sub-seasonal variability of supraglacial ice cliff melt rates and associated processes from time-lapse photogrammetry, Cryosphere, 10.5194/tc-16-4701-2022, 2022.

Kneib, M., Fyffe, C. L., Miles, E. S., Lindemann, S., Shaw, T. E., Buri, P., McCarthy, M., Ouvry, B., Vieli, A., Sato, Y., Kraaijenbrink, P. D. A., Zhao, C. X., Molnar, P., and Pellicciotti, F.: Controls on Ice Cliff Distribution and Characteristics on Debris-Covered Glaciers, Geophysical Research Letters, 50, 10.1029/2022gl102444, 2023.

King, O., Bhattacharya, A., Bhambri, R., and Bolch, T.: Glacial lakes exacerbate Himalayan glacier mass loss, Scientific Reports, 9, 10.1038/s41598-019-53733-x, 2019.

Kraaijenbrink, P., Meijer, S. W., Shea, J. M., Pellicciotti, F., De Jong, S. M., and Immerzeel, W. W.: Seasonal surface velocities of a Himalayan glacier derived by automated correlation of unmanned aerial vehicle imagery, Annals of Glaciology, 57, 103-113, 10.3189/2016AoG71A072, 2016.

Li, T., Zhang, B. G., Cheng, X., Westoby, M. J., Li, Z. H., Ma, C., Hui, F. M., Shokr, M., Liu, Y., Chen, Z. Q., Zhai, M. X., and Li, X. Q.: Resolving Fine-Scale Surface Features on Polar Sea Ice: A First Assessment of UAS Photogrammetry Without Ground Control, Remote Sensing, 11, 10.3390/rs11070784, 2019.

Maussion, F., Scherer, D., Molg, T., Collier, E., Curio, J., and Finkelnburg, R.: Precipitation Seasonality and Variability over the Tibetan Plateau as Resolved by the High Asia Reanalysis, Journal of Climate, 27, 1910-1927, 10.1175/jcli-d-13-00282.1, 2014.

McCarthy, M., Pritchard, H., Willis, I., and King, E.: Ground-penetrating radar measurements of debris thickness on Lirung Glacier, Nepal, Journal of Glaciology, 63, 543-555, 10.1017/jog.2017.18, 2017.

McSaveney, M.J., 1975. The Sherman Glacier Rock Avalanche of 1964: its Emplacement and Subsequent Effects on the Glacier beneath it. Ph.D. Ohio State University,Columbus, OH, p. 403.

Messerli, A. and Grinsted, A.: Image georectification and feature tracking toolbox: ImGRAFT, Geoscientific Instrumentation Methods and Data Systems, 4, 23-34, 10.5194/gi-4-23-2015, 2015.

Mihalcea, C., Mayer, C., Diolaiuti, G., D'Agata, C., Smiraglia, C., Lambrecht, A., Vuillermoz, E., and Tartari, G.: Spatial distribution of debris thickness and melting from remote-sensing and meteorological data, at debris-covered Baltoro glacier, Karakoram, Pakistan,

General Assembly of the International-Association-of-Geodesy/24th General Assembly of the International-Union-of-Geodesy-and-Geophysics, Perugia, ITALY, Jul 02-13, WOS:000257063000008, 49-+, 10.3189/172756408784700680, 2008.

Miles, E. S., Pellicciotti, F., Willis, I. C., Steiner, J. F., Buri, P., and Arnold, N. S.: Refined energy-balance modelling of a supraglacial pond, Langtang Khola, Nepal, Annals of Glaciology, 57, 29-40, 10.3189/2016AoG71A421, 2016.

Miles, E. S., Steiner, J., Willis, I., Buri, P., Immerzeel, W. W., Chesnokova, A., and Pellicciotti, F.: Pond Dynamics and Supraglacial-Englacial Connectivity on Debris-Covered Lirung Glacier, Nepal, Frontiers in Earth Science, 5, 10.3389/feart.2017.00069, 2017.

Miles, E. S., Steiner, J. F., Buri, P., Immerzeel, W. W., and Pellicciotti, F.: Controls on the relative melt rates of debris-covered glacier surfaces, Environmental Research Letters, 17, 10.1088/1748-9326/ac6966, 2022.

Miles, E. S., Willis, I., Buri, P., Steiner, J. F., Arnold, N. S., and Pellicciotti, F.: Surface Pond Energy Absorption Across Four Himalayan Glaciers Accounts for 1/8 of Total Catchment Ice Loss, Geophysical Research Letters, 45, 10464-10473, 10.1029/2018gl079678, 2018.

Miles, E., McCarthy, M., Dehecq, A., Kneib, M., Fugger, S., and Pellicciotti, F.: Health and sustainability of glaciers in High Mountain Asia, Nature Communications, 12, 10.1038/s41467-021-23073-4, 2021.

Mishra, N. B., Miles, E. S., Chaudhuri, G., Mainali, K. P., Mal, S., Singh, P. B., and Tiruwa, B.: Quantifying heterogeneous monsoonal melt on a debris-covered glacier in Nepal Himalaya using repeat uncrewed aerial system (UAS) photogrammetry, Journal of Glaciology, 68, 288-304, 10.1017/jog.2021.96, 2022.

Mölg, N., Bolch, T., Walter, A., and Vieli, A.: Unravelling the evolution of Zmuttgletscher and its debris cover since the end of the Little Ice Age, The Cryosphere, 13, 1889–1909, https://doi.org/10.5194/tc-13-1889-2019, 2019.

Mölg, N., Ferguson, J., Bolch, T., and Vieli, A.: On the influence of debris cover on glacier morphology: How high-relief structures evolve from smooth surfaces, Geomorphology, 357, 107092, https://doi.org/10.1016/j.geomorph.2020.107092, 2020.

Nakawo, M., Yabuki, H., and Sakai, A.: Characteristics of Khumbu Glacier, Nepal Himalaya: recent change in the debris-covered area, in: Annals of Glaciology, Vol 28, edited by: Kleman, J., Annals of Glaciology-Series, 118-122, 10.3189/172756499781821788, 1999.

Neckel, N., Loibl, D., and Rankl, M.: Recent slowdown and thinning of debris-covered glaciers in south-eastern Tibet, Earth and Planetary Science Letters, 464, 95-102, 10.1016/j.epsl.2017.02.008, 2017.

Nicholson, L. and Benn, D. I.: Calculating ice melt beneath a debris layer using meteorological data, Journal of Glaciology, 52, 463-470, 10.3189/172756506781828584, 2006.

Nuimura, T., Fujita, K., and Sakai, A.: Downwasting of the debris-covered area of Lirung Glacier in Langtang Valley, Nepal Himalaya, from 1974 to 2010, Quaternary International, 455, 93-101, 10.1016/j.quaint.2017.06.066, 2017.

Ostrem, G.: Ice Melting under a Thin Layer of Moraine, and the Existence of Ice Cores in Moraine Ridges, Geogr. Ann., 41, 228–230, 10.1080/20014422.1959.11907953, 1959.

Pellicciotti, F., Stephan, C., Miles, E., Herreid, S., Immerzeel, W. W., and Bolch, T.: Mass-balance changes of the debris-covered glaciers in the Langtang Himal, Nepal, from 1974 to 1999, Journal of Glaciology, 61, 373-386, 10.3189/2015JoG13J237, 2015.

Quincey, D. J., Richardson, S. D., Luckman, A., Lucas, R. M., Reynolds, J. M., Hambrey, M. J., and Glasser, N. F.: Early recognition of glacial lake hazards in the Himalaya using remote sensing datasets, Global and Planetary Change, 56, 137-152, 10.1016/j.gloplacha.2006.07.013, 2007.

Racoviteanu, A. E., Nicholson, L., Glasser, N. F., Miles, E., Harrison, S., and Reynolds, J. M.: Debris-covered glacier systems and associated glacial lake outburst flood hazards: challenges and prospects, Journal of the Geological Society, 179, 10.1144/jgs2021-084, 2022.

Reid, T. D. and Brock, B. W.: An energy-balance model for debris-covered glaciers including heat conduction through the debris layer, Journal of Glaciology, 56, 903-916, 10.3189/002214310794457218, 2010.

Reid, T. D. and Brock, B. W.: Assessing ice-cliff backwasting and its contribution to total ablation of debris-covered Miage glacier, Mont Blanc massif, Italy, Journal of Glaciology, 3439-3457, https://doi.org/10.3189/2014JoG13J045, 2014.

Reid, T. D., Carenzo, M., Pellicciotti, F., and Brock, B. W.: Including debris cover effects in a distributed model of glacier ablation, Journal of Geophysical Research-Atmospheres, 117, 10.1029/2012jd017795, 2012.

Rossini, M., Di Mauro, B., Garzonio, R., Baccolo, G., Cavallini, G., Mattavelli, M., De Amicis, M., and Colombo, R.: Rapid melting dynamics of an alpine glacier with repeated UAV photogrammetry, Geomorphology, 304, 159-172, 10.1016/j.geomorph.2017.12.039, 2018.

Rounce, D. R., Hock, R., McNabb, R. W., Millan, R., Sommer, C., Braun, M. H., Malz, P., Maussion, F., Mouginot, J., Seehaus, T. C., and Shean, D. E.: Distributed Global Debris Thickness Estimates Reveal Debris Significantly Impacts Glacier Mass Balance, Geophysical Research Letters, 48, 10.1029/2020gl091311, 2021.

Rowan, A. V., Egholm, D. L., Quincey, D. J., Hubbard, B., King, O., Miles, E. S., Miles, K. E., and Hornsey, J.: The Role of Differential Ablation and Dynamic Detachment in Driving Accelerating Mass Loss From a Debris-Covered Himalayan Glacier, Journal of Geophysical Research-Earth Surface, 126, 10.1029/2020jf005761, 2021.

Sakai, A. and Fujita, K.: Formation conditions of supraglacial lakes on debris-covered glaciers in the Himalaya, Journal of Glaciology, 56, 177-181, 10.3189/002214310791190785, 2010.

Sakai, A., Nakawo, M., and Fujita, K.: Distribution Characteristics and Energy Balance of Ice Cliffs on Debris-covered Glaciers, Nepal Himalaya, Arctic, Antarctic, and Alpine Research, 34, 12–19, 10.1080/15230430.2002.12003463, 2002.

Sakai, A., Nakawo, M., and Fujita, K.: Melt rate of ice cliffs on the Lirung Glacier, Nepal Himalayas, 1996, Bulletin of Glacier Research, 810 16, 57–66, 1998.

Sato, Y., Fujita, K., Inoue, H., Sunako, S., Sakai, A., Tsushima, A., Podolskiy, E. A., Kayastha, R., and Kayastha, R. B.: Ice Cliff Dynamics of Debris-Covered Trakarding Glacier in the Rolwaling Region, Nepal Himalaya, Frontiers in Earth Science, 9, 10.3389/feart.2021.623623, 2021.

Scherler, D., Wulf, H., and Gorelick, N.: Global Assessment of Supraglacial Debris-Cover Extents, Geophysical Research Letters, 45, 11798-11805, 10.1029/2018gl080158, 2018.

Shean, D. E., Bhushan, S., Montesano, P., Rounce, D. R., Arendt, A., and Osmanoglu, B.: A Systematic, Regional Assessment of High Mountain Asia Glacier Mass Balance, Frontiers in Earth Science, 7, 10.3389/feart.2019.00363, 2020.

Shugar, D. H. and Clague, J. J.: The sedimentology and geomorphology of rock avalanche deposits on glaciers, Sedimentology, 58, 1762-1783, 10.1111/j.1365-3091.2011.01238.x, 2011.

Steiner, J. F., Buri, P., Miles, E. S., Ragettli, S., and Pellicciotti, F.: Supraglacial ice cliffs and ponds on debris-covered glaciers: spatio-temporal distribution and characteristics, Journal of Glaciology, 65, 617-632, 10.1017/jog.2019.40, 2019.

Steiner, J. F., Pellicciotti, F., Bur, P., Miles, E. S., Immerzeel, W. W., and Reid, T. D.: Modelling ice-cliff backwasting on a debris-covered glacier in the Nepalese Himalaya, Journal of Glaciology, 61, 889-907, 10.3189/2015JoG14J194, 2015.

Tadono, T., Ishida, H., Oda, F., Naito, S., Minakawa, K., and Iwamoto, H.: Precise Global DEM Generation by ALOS PRISM, ISPRS Ann. Photogramm. Remote Sens. Spatial Inf. Sci., II-4, 71–76, https://doi.org/10.5194/isprsannals-II-4-71-2014, 2014.

Thompson, S., Benn, D. I., Mertes, J., and Luckman, A.: Stagnation and mass loss on a Himalayan debris-covered glacier: processes, patterns and rates, J. Glaciol., 62, 467–485, https://doi.org/10.1017/jog.2016.37, 2016.

Van der Veen, C.J. (2013). Fundamentals of Glacier Dynamics (2nd ed.). CRC Press. https://doi.org/10.1201/b14059.

Van Tricht, L., Huybrechts, P., Van Breedam, J., Vanhulle, A., Van Oost, K., and Zekollari, H.: Estimating surface mass balance patterns from unoccupied aerial vehicle measurements in the ablation area of the Morteratsch-Pers glacier complex (Switzerland), Cryosphere, 15, 4445-4464, 10.5194/tc-15-4445-2021, 2021.

Vincent, C., Ramanathan, A., Wagnon, P., Dobhal, D. P., Linda, A., Berthier, E., Sharma, P., Arnaud, Y., Azam, M. F., Jose, P. G., and Gardelle, J.: Balanced conditions or slight mass gain of glaciers in the Lahaul and Spiti region (northern India, Himalaya) during the nineties preceded recent mass loss, Cryosphere, 7, 569-582, 10.5194/tc-7-569-2013, 2013.

Vincent, C., Wagnon, P., Shea, J. M., Immerzeel, W. W., Kraaijenbrink, P., Shrestha, D., Soruco, A., Arnaud, Y., Brun, F., Berthier, E., and Sherpa, S. F.: Reduced melt on debris-covered glaciers: investigations from Changri Nup Glacier, Nepal, Cryosphere, 10, 1845-1858, 10.5194/tc-10-1845-2016, 2016.

Wang, W. C., Yao, T. D., and Yang, X. X.: Variations of glacial lakes and glaciers in the Boshula mountain range, southeast Tibet, from the 1970s to 2009, Annals of Glaciology, 52, 9-17, 10.3189/172756411797252347, 2011.

Westoby, M. J., Brasington, J., Glasser, N. F., Hambrey, M. J., and Reynolds, J. M.: 'Structure-from-Motion' photogrammetry: A low-cost, effective tool for geoscience applications, Geomorphology, 179, 300-314, 10.1016/j.geomorph.2012.08.021, 2012.

Westoby, M. J., Rounce, D. R., Shaw, T. E., Fyffe, C. L., Moore, P. L., Stewart, R. L., and Brock, B. W.: Geomorphological evolution of a debris-covered glacier surface, Earth Surface Processes and Landforms, 45, 3431-3448, 10.1002/esp.4973, 2020.

Wigmore, O. and Mark, B.: Monitoring tropical debris-covered glacier dynamics from high-resolution unmanned aerial vehicle photogrammetry, Cordillera Blanca, Peru, Cryosphere, 11, 2463-2480, 10.5194/tc-11-2463-2017, 2017.

Xu, S. Y., Fu, P., Quincey, D., Feng, M. L., Marsh, S., and Liu, Q.: UAV-based geomorphological evolution of the Terminus Area of the Hailuogou Glacier, Southeastern Tibetan Plateau between 2017 and 2020, Geomorphology, 411, 10.1016/j.geomorph.2022.108293, 2022

Yang, W., Guo, X. F., Yao, T. D., Zhu, M. L., and Wang, Y. J.: Recent accelerating mass loss of southeast Tibetan glaciers and the relationship with changes in macroscale atmospheric circulations, Climate Dynamics, 47, 805-815, 10.1007/s00382-015-2872-y, 2016.

Yang, W., Yao, T. D., Guo, X. F., Zhu, M. L., Li, S. H., and Kattel, D. B.: Mass balance of a maritime glacier on the southeast Tibetan Plateau and its climatic sensitivity, Journal of Geophysical Research-Atmospheres, 118, 9579-9594, 10.1002/jgrd.50760, 2013.

Yang, W., Yao, T. D., Zhu, M. L., and Wang, Y. J.: Comparison of the meteorology and surface energy fluxes of debris-free and debris-covered glaciers in the southeastern Tibetan Plateau, Journal of Glaciology, 63, 1090-1104, 10.1017/jog.2017.77, 2017.

Yang, W., Zhao, C. X., Westoby, M., Yao, T. D., Wang, Y. J., Pellicciotti, F., Zhou, J. M., He, Z., and Miles, E.: Seasonal Dynamics of a Temperate Tibetan Glacier Revealed by High-Resolution UAV Photogrammetry and In Situ Measurements, Remote Sensing, 12, 10.3390/rs12152389, 2020.

Yao, T. D., Thompson, L., Yang, W., Yu, W. S., Gao, Y., Guo, X. J., Yang, X. X., Duan, K. Q., Zhao, H. B., Xu, B. Q., Pu, J. C., Lu, A. X., Xiang, Y., Kattel, D. B., and Joswiak, D.: Different glacier status with atmospheric circulations in Tibetan Plateau and surroundings, Nature Climate Change, 2, 663-667, 10.1038/nclimate1580, 2012.

Ye, D. and Gao, Y.: Meteorology of the Tibetan Plateau, Science Press, Beijing, 1979.

Zhang, Y., Fujita, K., Liu, S. Y., Liu, Q., and Nuimura, T.: Distribution of debris thickness and its effect on ice melt at Hailuogou glacier, southeastern Tibetan Plateau, using in situ surveys and ASTER imagery, Journal of Glaciology, 57, 1147-1157, 10.3189/002214311798843331, 2011.

Zhang, Y., Hirabayashi, Y., Fujita, K., Liu, S. Y., and Liu, Q.: Heterogeneity in supraglacial debris thickness and its role in glacier mass changes of the Mount Gongga, Science China-Earth Sciences, 59, 170-184, 10.1007/s11430-015-5118-2, 2016.

Zhao, C. X., Yang, W., Westoby, M., An, B. S., Wu, G. J., Wang, W. C., Wang, Z. Y., Wang, Y. J., and Dunning, S.: Brief communication: An approximately 50 Mm^3 ice-rock avalanche on 22 March 2021 in the Sedongpu valley, southeastern Tibetan Plateau, Cryosphere, 16, 1333-1340, 10.5194/tc-16-1333-2022, 2022.

Zhong, Y., Liu, Q., Westoby, M., Nie, Y., Pellicciotti, F., Zhang, B., Cai, J. L., Liu, G. X., Liao, H. J., and Lu, X. Y.: Intensified paraglacial slope failures due to accelerating downwasting of a temperate glacier in Mt. Gongga, southeastern Tibetan Plateau, Earth Surface Dynamics, 10, 23-42, 10.5194/esurf-10-23-2022, 2022.

Data availability

The UAV-derived orthomosaics and DEMs of this study are openly available in Zenodo at https://doi.org/10.5281/zenodo.7350479. The above data will be available when this paper is final published in TC.

Author Contributions

CZ, WY, ESM, MW, MK, FP designed the study and completed the data analysis. WY supervised the study. WY, CZ, ESM, MW, MK, YW, ZH conducted the fieldwork. All authors contributed to the writing and revision of the paper.

Funding

The study is supported by the Second Tibetan Plateau Scientific Expedition and Research Program (STEP) (2019QZKK0201), the National Natural Science Foundation of China (41961134035), the Royal Society Newton Advanced Fellowship (NA170325) and National Key Research and Development Project (2019YFC1509102).

Acknowledgements

We additionally acknowledge the support of CNES (Centre National d'Etudes Spatiales) via the DINAMIS project for facilitating access to Pléiades imagery through an academic agreement. We are grateful to RESTEC for AW3D DEM. We thank for Romain Hugonnet et al. and Amaury Dehecq et al. for their datasets of glacier surface elevation change and velocity. We would like to thank Martin Truffer for collecting and providing the ice thickness data of 24K Glacier. We thank Thomas Shaw, Catriona Fyffe, Michael McCarthy, Pascal Buri, Achille Jouberton, Yota Sato, Stefan Fugger and Rebecca Stewart for their guidance and help.

Competing interests

The authors have the following competing interests: At least one of the coauthors is a member of the editorial board of The Cryosphere.